Droplet Behaviour on Superhydrophobic surfaces

Yifei Bian

Supervised by Professor I. P. Parkin and C. J. Carmalt

Department of Chemistry, University College London 2019

Thesis Submitted in Partial Fulfilment of the Requirements

for the Degree of Doctor of Philosophy

Declaration

I, Yifei Bian, confirm that the work presented in this thesis is my own. Where information has been derived from other sources, I confirm that this has been indicated in the thesis.

Abstract

Superhydrophobic surfaces, implied by its name, refer to 'ultra-water-repellent surfaces'. They were observed in nature and researched by people for their intrinsic mechanism behind low water adhesion. Massive researches have been conducted recently for novel fabrications and further applications of superhydrophobic surfaces. This thesis will start from the synthesis, then present studies on several behaviours of water droplets on surfaces, including sliding, evaporation and collision.

Firstly, a new synthesis approach of superhydrophobic thin films by modification of a Co_3O_4 film was illustrated. The surface morphology could be controlled by the reaction time, and the investigation into the relationship between the water contact angle, sliding angle, droplet size and surface micro-structures showed that the water-surface adhesion can be effectively manipulated through tailoring the morphology or the size of the micro-structures of the surfaces.

After that, evaporation of water droplets was studied as a dynamic behaviour, and the effect of temperature was taken into account. An experimental and theoretical understanding of the evaporation of sessile water droplets was reported at different static water contact angles on hydrophobic and superhydrophobic substrates. With the assumption that two evaporation modes, constant contact radius (CCR) mode and constant contact angle (CCA) mode dominate successively during the process the lifetime of the droplets was analyzed with substrate temperature. The result shows that generally the lifetime increases as surface contact angle rises whereas it decreases when the temperature rises. Evaporative cooling effect was taken into consideration and shown to have a minor influence on the process.

Finally, the thesis reports another water droplet behaviour. The coalescence and rebound process of binary droplets with different temperatures on superhydrophobic surface were studied. During the experiments, a 'stationary' droplet was kept on a superhydrophobic surface at room temperature and an 'impacting' droplet with temperature ranging from room temperature to 70 ℃ was released from above. The findings reveal that an increase in the temperature of the impacting droplet facilitated the coalescence process between the binary droplets. When both the temperatures of the impacting droplet and of the stationery were at room-temperature, a large deformation was observed before merging, while the deformation reduced as the temperature of the 'impacting' droplet increased. Energy dissipation was also considered in the study.

Impact Statement

Superhydrophobic surface is kind of surface with special properties of high water-repellence and self-cleaning. The Lotus Plant is one of the examples in nature, and its water-resistant behaviour is named 'The Lotus Effect'. It has been revealed that the low water adhesion comes from micro- and nano- structures of these surfaces. Laboratory studies have been done exploring new fabrication approaches, such as more economically or environmentally friendly methods, and possible applications of the surfaces, from waterproof fabrics and oil-water separation, to anti-bacteria coatings.

In this thesis, a novel synthesis method was first introduced, based on the growth of Co_3O_4 micro-architecture on an aluminium sheet. After that, the substrate was modified by a simple immersion step to gain superhydrophobicity. Also, it was observed that the surface morphology could be easily controlled by adjusting the time of growth step. The route can therefore be adopted as a low-cost method to generate sample surfaces with evolutional morphology for testing use.

Following this, some behaviours of water droplets on superhydrophobic surfaces were studied, including contact and sliding angles, evaporation and collision. The findings suggest that surface morphology has a great impact on the static behaviours and droplet temperature is a dominating factor during dynamic processes, which help further evaluate the natural phenomena of water droplet and may offer solutions to some industrial problems such as deposition and droplets adhesion.

Acknowledgement

Contents

List of figures

Chapter 1. Introduction

Fig. 1.1 (a) Water droplet wetting on a wax-coated glass substrate. (b) on an untreated glass substrate. (c) on a plasma-cleaned glass substrate.

Fig 1.2 (a) Photo of raindrops sitting on Lotus leaves. (b) An SEM image of a Lotus leaf showing the micro protrusions and structures that makes a rough surface. Bar: 20 µm. (c) and (d) demonstrate the difference between a rolling droplet on a smooth surface and a water-repellent rough surface. In (d) the dirt particles are picked up and taken away as the droplet rolls down.

Fig. 1.3 Nelumbo Nucifera which is reported to have anti-bacterial activity against food-borne pathogens.

Fig. 1.4 Molecular environment in the bulk and at the interface. The molecules in the bulk are surrounded by other molecules in all directions so that the cohesive force cancelled with each other. However, those at the interface experience only net inward cohesive force.

Fig. 1.5 Water drops leaking from a tap. Water adhering to the tap gains mass until it is stretched to a point where the surface tension can no longer keep the drop linked to the tap. It then separates and surface tension forms the drop into a sphere.

Fig. 1.6 Principal radii of curvature of a liquid drop.

Fig. 1.7 Scheme of Young's model on contact angle.

Fig. 1.8 Scheme of (a) Cassie-Baxter Model and (b) Wenzel Model.

Fig. 1.9 Surfaces in different wettability. (a) A glass slide surface (water contact angle, 11.0°). (b) A plastic film surface (water contact angle, 106.2°). (c) A filter paper surface (water contact angle, ~0°). (d) A glass substrate painted with superhydrophobic coating (water contact angle, 165.6°). The size of water droplets is ~5 µL.

Fig. 1.10 (a) SEM image of a polystyrene surface modified by polystyrene beads, with a diameter of 400 nm. WCA=135°. (b) SEM image of a 440-nm-diameter double-layer polystyrene surface after 120s of oxygen plasma treatment, WCA = 170°. Bar = 1μm.

Fig. 1.11 Schematic set-up of measuring contact angle with contact angle goniometer, from side view.

Fig. 1.12 Sliding angle of a surface is defined as the tilted angle of the substrate below when the droplet starts to slide.

Fig. 1.13 (a, b) SEM images of the surface of a red rose petal, showing a periodic array of micropapillae and nanofolds on each papillae top. (c) Shape of a water droplet on the petal's surface, indicating its superhydrophobicity with a contact angle of 152.4°. (d) Shape of water on the petal's surface when it is turned upside down.

Fig. 1.14 Demonstration of advancing and receding contact angles (θ_a, θ_r), surface tension (γ) and gravitational force (mg) for a droplet on a surface tilted at sliding angle (θ_{SA}).

Fig. 1.15 Schemes of the captive-drop goniometry when measuring (a) the advancing contact angle and (b) the receding contact angle.

Chapter 2. Synthesis of superhydrophobic surfaces with Wenzel and Cassie–Baxter states

Fig. 2.5 (a) XPS spectra for the obtained film surface before and after stearic acid modification. (b) The spectrum of Co2p. (c) The decomposed spectrum of O1s after stearic acid modification. (d) C1s spectrum before and after surface modification.

Fig. 2.6 The relationship between contact angle (a) and sliding angle (b) values and droplet volume on different surfaces with reaction times of 13 h (S1), 16 h (S2), and 18 h (S3). The volume of droplets inset in (a) from left to right is 0.5, 1, 2, 4, 6, 8, 10 μL.

Fig. 2.7 Force−distance curves on the superhydrophobic surfaces under reaction times of 13 h (a), 16 h (b), and 18 h (c). The relationship between the adhesive force and the droplet volume is shown in (d). (e) gives an illustration of the 3 steps.

Fig. 2.8 Sine value of the sliding angle plotted against $V^{-1/3}$. ▲, ● and ■ represent actual data points, and the dotted lines equal the theoretical calculation.

Chapter 3. **Lifetime of droplets evaporation on hydrophobic surfaces**

Fig. 3.1 diagram of droplet evaporation

Fig. 3.2 The assumed uniform outer diffusion flux from droplet surface.

Fig. 3.3 Evaporation lifetime of water droplets on three different substrates, experiment data.

Fig. 3.4 Experimental and CCA-modelling droplets lifetime on three substrates. When CA = 164.8°, all three curves descend with temperature and the experimental curve almost follows the stages of the Erbil-CCA one.

Fig. 3.5 The curves of $t_{total} - \theta$ are plotted at experimental data points to find out the value of θ_t.

Fig. 3.6 θ_t at which CCR stage transits to CCA state on different substrates.

List of Tables

Chapter 3. Lifetime of droplets evaporation on heated hydrophobic surfaces

List of Equations

Chapter 1. Introduction

(1.1) Young-Laplace equation

(1.2) Simplification of Young-Laplace equation

(1.3) Young' relation on contact angle

(1.4) Wenzel model

(1.5) Cassie-Baxter model

(1.6) Simplification of Cassie-Baxter model

(1.7) Contact angle hysteresis

(1.8) Relationship between the advancing contact angle, the receding contact angle and the sliding angle

Chapter 2. Synthesis of superhydrophobic surfaces with Wenzel and Cassie–Baxter state

(2.1) Young's relation, Wenzel model and Cassie-Baxter model

(2.2) Volume of a spherical cap

(2.3) Contact radius of a drop

(2.4) Relationship between contact angles and sliding angles on a rough surface

(2.5) Simplification of the relationship between contact angle and sliding angle

Chapter 4. Binary Impacting droplets on superhydrophobic surface

List of Abbreviations

AACVD   Aerosol-assisted chemical vapour deposition

CA   Contact angle

CAH   Contact angle hysteresis

CCA   Constant Contact Angle

CCR   Constant Contact Radius

CVD   Chemical vapour deposition

CDG   Captive-drop goniometry

FESEM   Field emission scanning electron microscopy

RA   Rolling angle

SA   Sliding angle

SH   Superhydrophobic

SEM   Scanning electron microscopy

TA   Tilting angle

TEM   Transmission electron microscopy

TPG   Tilting-plate goniometry

WCA   Water contact angle

XRD   X-ray diffractometer

XPS   X-ray photoelectron spectroscopy

Chapter 1. Introduction

1.1 Wetting and partial-wetting

Wetting is a very natural phenomenon in people's daily life, such as laundry or drinking. Generally, wetting is the ability of a liquid to maintain contact with a solid surface. Particularly, wetting is seen in the spreading of a liquid over a solid surface in contact with a gas or other liquid and determines the shape of a droplet on a solid surface. Imagine a water drop deposited on a very clean glass substrate which will spread out flatly and, by contrast, another one placed on a wax raincoat forming a semi-spherical shape. It can be seen that there exist two regimes of wetting. One is total wetting, when the liquid has a strong adhesion with the solid substrate; and partial wetting, the opposite case.
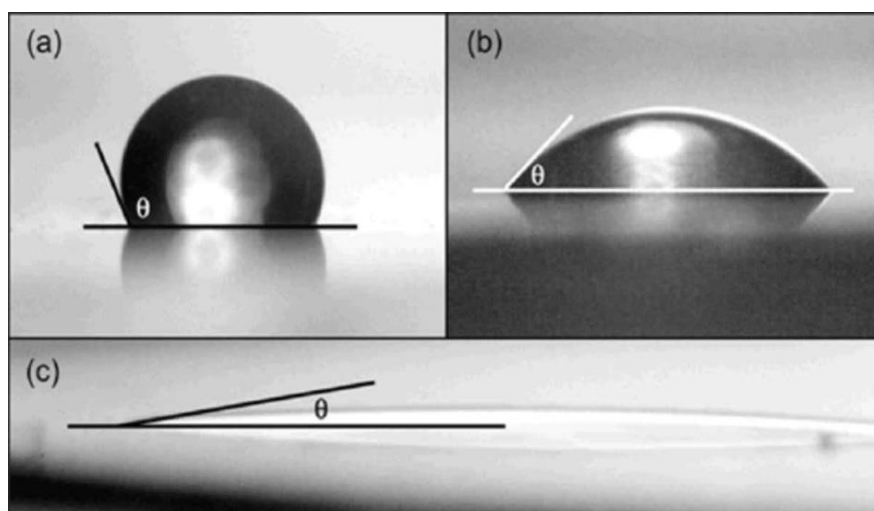
Fig 1.1 (a) Water droplet wetting on a wax-coated glass substrate. (b) on an untreated glass substrate. (c) on a plasma-cleaned glass substrate.[1] Figures reproduced with permission from Ref. 1.

Wetting is often regarded as a result of intermolecular interactions between liquid and solid in the zone of contact of three phases. An understanding of the intrinsic theories of the reason, the transformation, the replication and the applications of

wetting and partial-wetting will benefit people's life in many aspects. This thesis introduces an extremely water-repellent (superhydrophobic) surface and some behaviour of the water droplets, including evaporation, sliding and collision on the surface.

This chapter will give a brief introduction to the origin of non-wettable materials in nature, how people learn from the microstructure of these materials to summarize and replicate a bio-inspired surface and their applications.

1.1.1 The Lotus Effect

Some animals and plants in nature have special non-wetting properties for their own survival or for food-hunting. One of the most common examples is the well-known Lotus Plant.

From ancient to modern times, the lotus plant is considered as a symbol of purity in China, as it is rooted in the muddy bottoms of ponds and riverbeds while its leaves remain unpolluted despite any raindrops and dirt. Raindrops that fall onto them bead up and roll off down the surface, as shown in Fig. 1.2(a).

The water-repellent property comes from the micro- and nano-structures of the leaf surface (Fig 1.2(b)) which make the surface quite rough at nanoscale and minimize the droplets' adhesion to the surface[2,3]. Also, the nano-architectures are coated with a layer of superimposed hydrophobic wax to further reduce the water affinity[4-6].
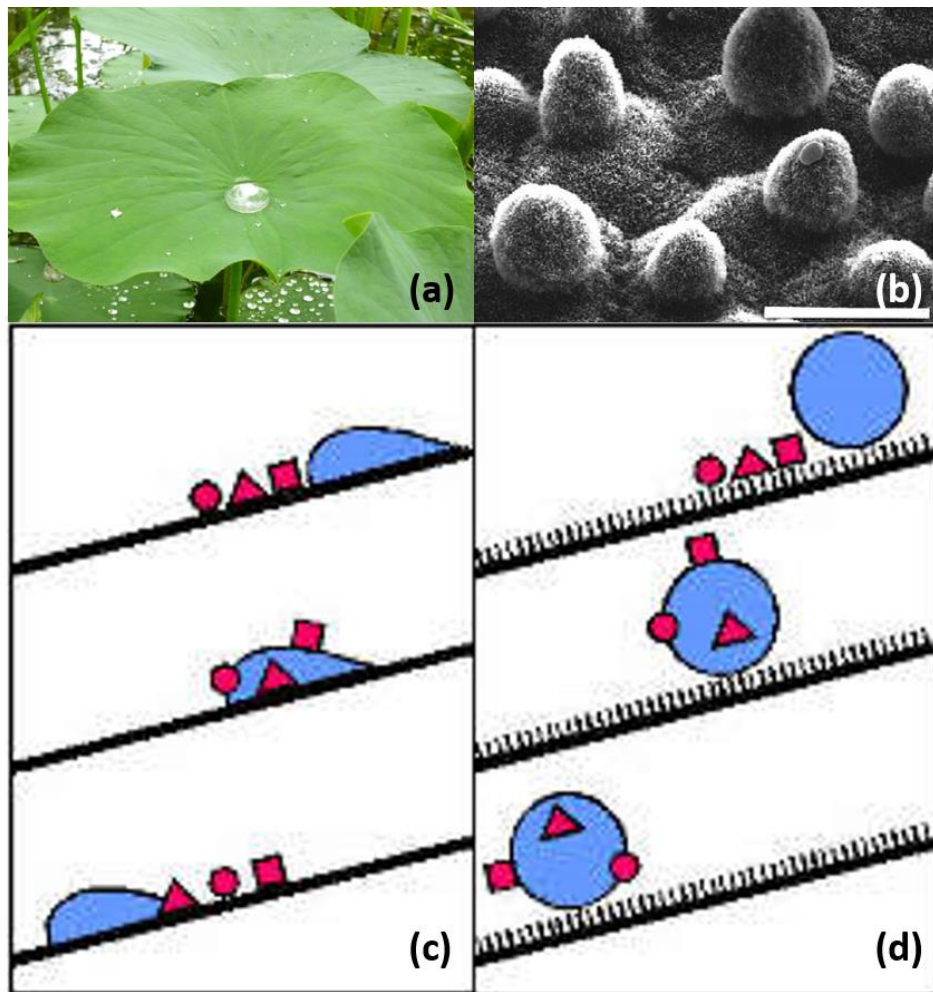
Fig 1.2 (a) Photo of raindrops sitting on Lotus leaves. (b) An SEM image of a Lotus leaf showing the micro protrusions and structures that makes a rough surface. Bar: 20 μm. (c) and (d) demonstrate the difference between a rolling droplet on a smooth surface and a water-repellent rough surface. In (d) the dirt particles are picked up and taken away as the droplet rolls down. (Figures reproduce with permission from Ref. 2)

Due to the extremely water-repellent property of the leaf surface, muddy water coming from its ambient aqueous environment just cannot stay on or stain the leaf surface. Besides, these leaves not only stay dry, but the droplets pick up small particles of dirt as they roll. This is called the self-cleaning property of the surface, including stain repellence and dirt removal.

Fig. 1.2(c) and (d) show the diagrams of droplets rolling down two contaminated surfaces and the mechanism of the dirt-removal process. In Fig. 1.2(c), the dirt particles are merely redistributed by rolling water droplets on a smooth surface. However, on a rough water-repellent surface in Fig. 1.2(d), dirt particles can be easily picked up and cleaned off by the rolling droplet[7,8]. This ultra-water-repellent and self-cleaning phenomenon of the lotus plant is called the Lotus Effect.

In nature, the Lotus plant is not the only case which illustrates the 'Lotus Effect'. For some plants the rough surface acts as an important protection against pathogens like fungi or bacteria. In addition, for some other plants the self-cleaning property is required to avoid the contamination of their surface area exposed to sunlight, which could lead to a reduction of photosynthesis[9].
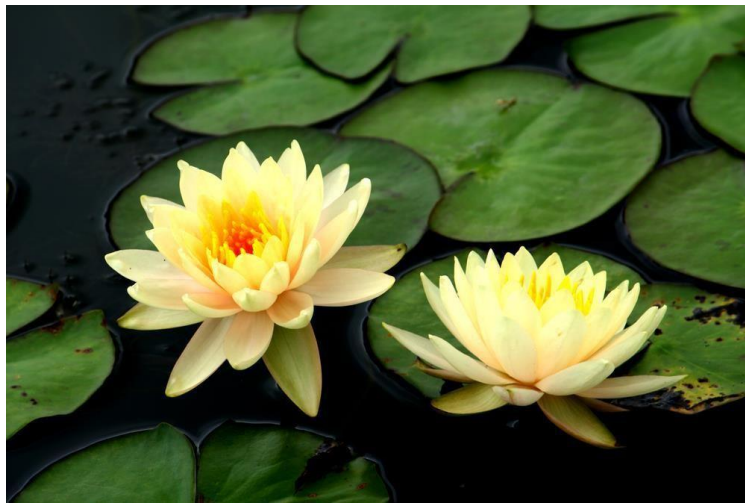
Fig. 1.3 Nelumbo Nucifera which is reported to have anti-bacterial activity against food-borne pathogens.

1.1.2 Surface tension

Surface tension is a force which makes liquid surface to shrink into the minimum surface area and it is believed to be the reason behind water-repellence phenomena on a lotus-like surface[10].
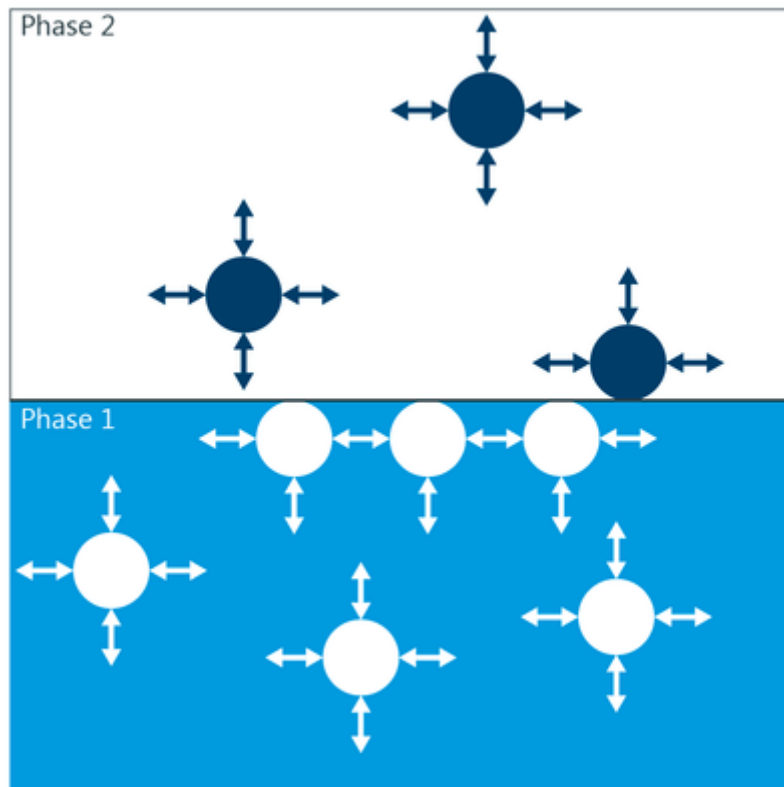
Fig 1.4 Molecular environment in the bulk and at the interface. The molecules in the bulk are surrounded by other molecules in all directions so that the cohesive force cancelled with each other. However, those at the interface experience only net inward cohesive force.[11] Figures reproduce with permission from Ref. 11.

The forces of attraction acting between the molecules of same type are called cohesive forces while those acting between the molecules of different types are called adhesive forces. As shown in Fig. 1.4, the surface tension results from an imbalance of intermolecular cohesive forces between molecules. Molecules in the interior of a liquid are attracted equally in all directions by neighbouring molecules, while molecules at the liquid surface have only net inward cohesive forces. The unbalanced attraction of molecules at the surface of a liquid tends to pull the molecules back into the bulk liquid leaving the minimum number of molecules on the

surface[12]. It required energy to increase the surface area of a liquid because a larger surface area contains more molecules in the unbalanced situation.
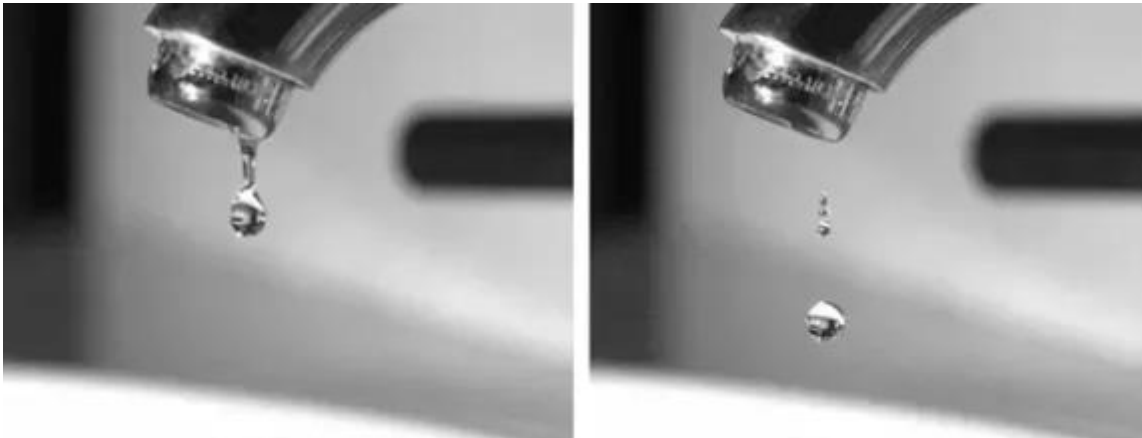
Fig. 1.5 Water adhering to the tap becomes larger until it is extended to a point where the surface tension can no longer keep the drop attached to the tap. The drop will then separate and form a spherical shape due to the surface tension.

That is why a water droplet will form a nearly spherical shape on a Lotus-like water-repellent surface. Since cohesion energy is often more than double of adhesion energy[13], and the adhesion energy is significantly reduced due to both the hydrophobic wax layer and low contact ratio between water droplets and the surface, cohesive force dominates the liquid-solid interaction at the surface. In fact, when cohesive force dominates, water droplets or virtually all liquid drops shrink into a spherical shape (as a sphere has minimal surface area) because of the imbalance in the cohesive force at the surface layer[14]. This leads to the non-wetting or water-repellent behaviour of the surface.

The relationship between the droplets shape, or radii of curvature, and the surface tension is described by Young-Laplace equation[15]:

$$\Delta p = \gamma \left(\frac{1}{R_1} + \frac{1}{R_2} \right) \qquad (1.1)$$

where Δp is called the Laplace pressure, the pressure difference across the liquid-gas interface, γ is the surface tension, R_1 and R_2 are the principal radii of curvature.
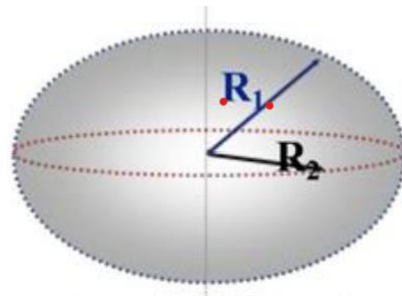
Fig. 1.6 Principal radii of curvature of a liquid drop.

In the case of spherical shapes, $R_1=R_2=R$, which simplifies the equation into:

$$\Delta p = \frac{2\gamma}{R} \qquad (1.2)$$

This demonstrates that shrinkage or decrease in radii of curvature of the droplet minimizes the surface tension.

1.1.3 Contact angle

The hydrophobicity, or the degree of non-wettability of a surface can be characterized by its contact angle, CA[16-18]. Higher contact angle means higher hydrophobicity or water-repellent capability.
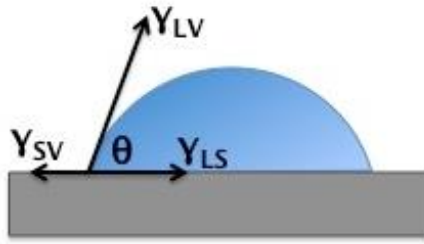
Fig. 1.7 Scheme of Young's model on contact angle.

The contact angle can be obtained via Young's model[19], as shown in Fig. 1.6. On the contact line of triple phases (liquid, gas, solid), the sum of capillary force or total interfacial energy should be zero.

If the solid–vapor interfacial energy is denoted by γ_{SV}, the liquid-solid interfacial energy by γ_{LS}, and the liquid–vapor interfacial energy (i.e. the surface tension) by γ_{LV}, by projecting the equilibrium forces on the solid plane, one obtains the Young' relation:

$$\gamma_{LS} - \gamma_{SV} + \gamma_{LV} \cdot \cos\theta_Y = 0 \qquad (1.3)$$

where θ_Y is the contact angle in this model.

Application of this equation is limited to an ideal surface that is rigid, perfectly flat and homogeneous. However, since all the real surfaces are not ideal, models were developed to describe the contact angles on the real surfaces.

There are two main models to describe the contact angle on a real surface, i.e. the Wenzel model[20, 21] and the Cassie-Baxter model[22, 23]. Contrary to the ideal surface, the real surface can have chemical heterogeneity and surface roughness.

In the Wenzel model, the surface roughness r is defined as the ratio of the actual area to the projected area of the surface and is normally greater than 1. The Wenzel equation can be written as:

$$\cos \theta_W = r \cdot \cos \theta_Y \qquad (1.4)$$

where θ_W is the apparent contact angle and θ_Y is the aforementioned equilibrium contact angle from Young's equation on a perfectly smooth surface.
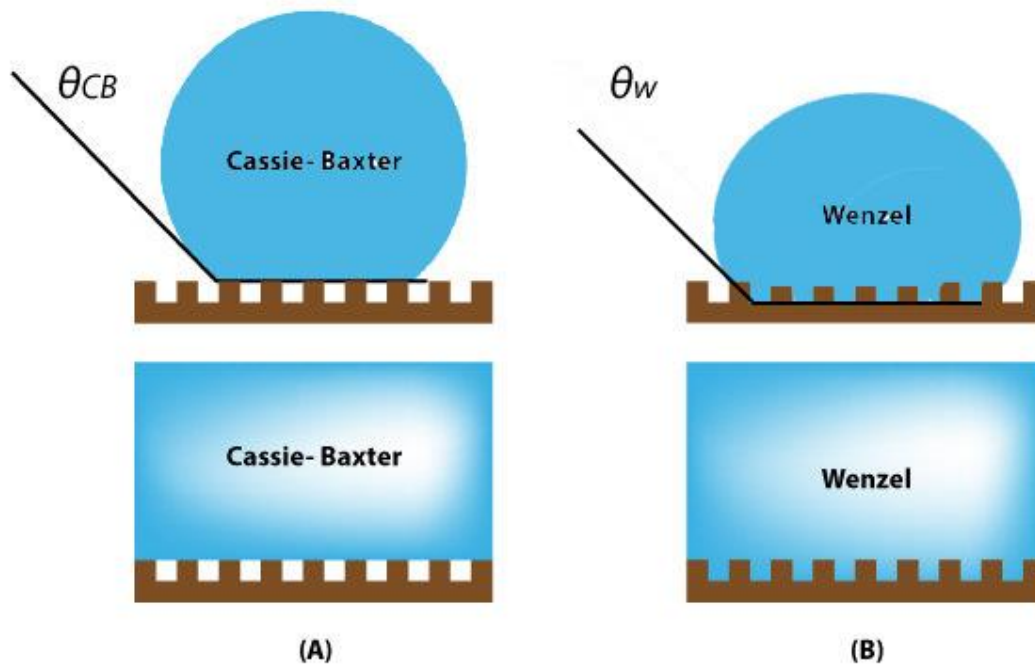
Fig. 1.8 Scheme of (a) Cassie-Baxter Model[22, 23] and (b) Wenzel Model[20, 21].

In the Cassie-Baxter model, droplets are supposed to stand on the surface roughness and air pockets between the protrusions, so that their contact with the solid substrate is avoided. The Cassie-Baxter equation can be written as:

$$\cos \theta_{CB} = f_s \cdot \cos \theta_s + f_v \cdot \cos \theta_v \qquad (1.5)$$

where f_s and f_v are respectively the area fractions of solid and air under the droplet on the surface. Considering $f_s + f_v = 1$, the equilibrium contact angle between droplets and surrounding vapor is a constant of 180°, and the equilibrium contact angle of the droplets on solid substrate equals to Young's θ_Y, the Cassie-Baxter equation can be simplified as:

$$\cos \theta_{CB} = f_s(1 + \cos \theta_Y) - 1 \qquad (1.6)$$

From the Wenzel model, it can be deduced that the surface roughness r amplifies the wettability of the original surface. Hydrophilic surface becomes more hydrophilic and hydrophobic surface more hydrophobic. In the Cassie-Baxter model, the area fractions under the droplet is important in that the larger the area fraction of air, the higher the contact angle. Although these two models were proposed over half a century ago, these equations have been widely used recently with active research on superhydrophobic surface.

As mentioned, water contact angle, WCA, is often used to characterize the wettability of a surface. Generally, if the water contact angle is smaller than 90°, the solid surface is considered wettable, or hydrophilic; if the water contact angle is larger than 90°, the solid surface is considered non-wettable, or hydrophobic[24-26]. Specifically, those surfaces whose water contact angles are greater than 150° are named superhydrophobic surfaces, which means they are extremely water-repellent and only very small part of the droplet surface is in contact with the substrate[27-29]. For example, Plants with a double structured surface like the lotus can reach a static contact angle of 170°, whereby the droplet's contact area is only 0.6%[30].

One of the common materials which show a hydrophobic surface is polymer. Some fluorinated polymers can have water contact angles of 130° due to their extremely low surface energies[32]. If the surface is further modified, such as roughening in certain ways, it may be able to show superhydrophobicity. Fig. 1.9 shows an example[33].
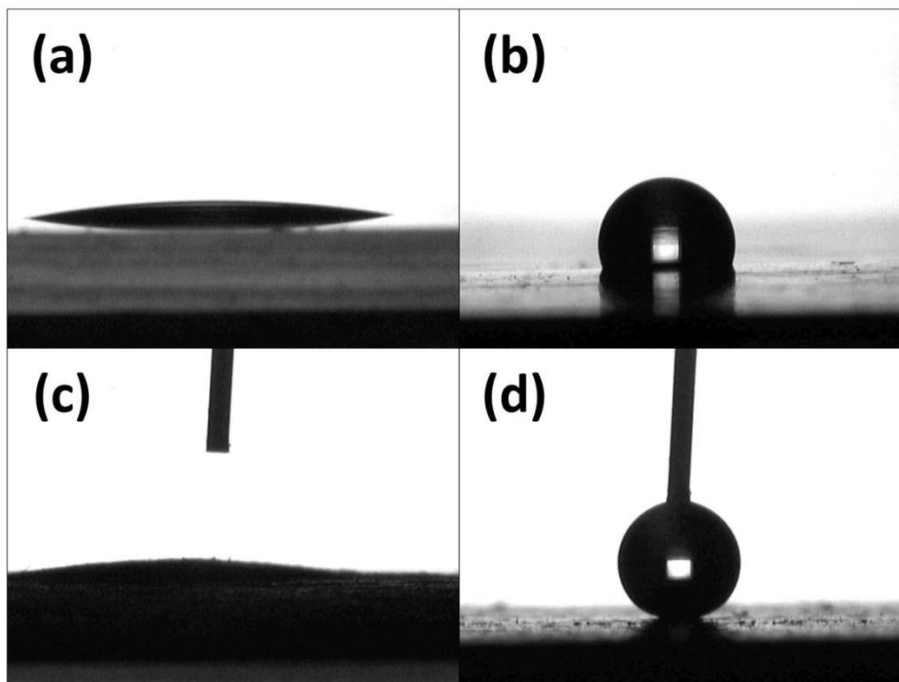
Fig. 1.9 Surfaces in different wettability. (a) A glass slide surface (water contact angle, 11.0°). (b) A plastic film surface (water contact angle, 106.2°). (c) A filter paper surface (water contact angle, ~0°). (d) A glass substrate painted with superhydrophobic coating (water contact angle, 165.6°). The size of water droplets is ~5 μL. Figures reproduce with permission from Ref. 31.

The most commonly used method of measuring the contact angle of a sessile drop is with a contact angle goniometer, which allows the user to measure the contact angle visually[34]. A droplet is deposited by a syringe which is positioned above the sample

surface, and a high-resolution camera captures the image from the profile or side view. The image can then be analysed either by eye (with a protractor) or more often is measured using image analysis software. This type of measurement is referred to as a static contact angle measurement. Although there might be some shortcomings like the influence of gravitational force and that the contact angle of the droplet placed in this method will be actually between equilibrium contact angle and advancing contact angle[35], the method is still widely adopted due to simplicity and convenience.
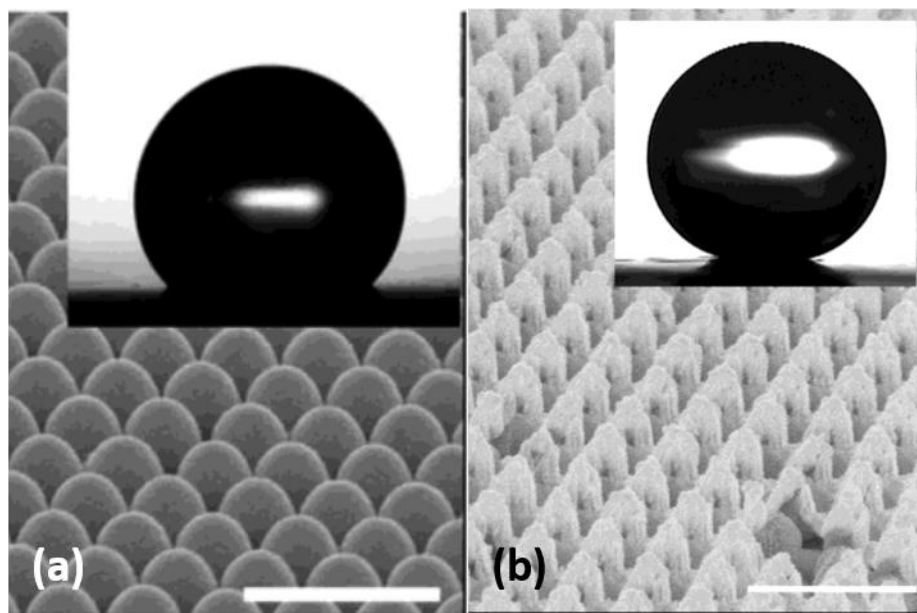
Fig. 1.10 (a) SEM image of a polystyrene surface modified by polystyrene beads, with a diameter of 400 nm. WCA=135°. (b) SEM image of a 440-nm-diameter double-layer polystyrene surface after 120s of oxygen plasma treatment, WCA = 170°. Bar=1µm. Figures reproduce with permission from Ref. 33.
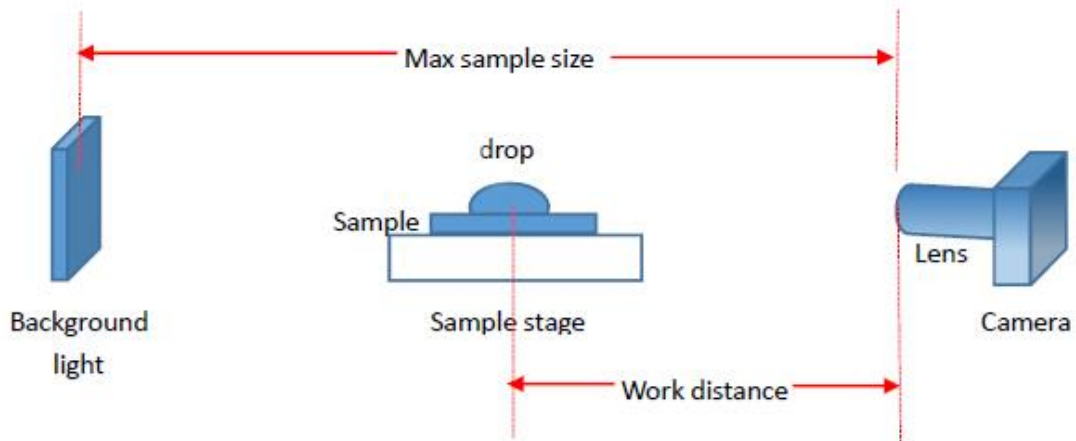
Fig. 1.11 Schematic set-up of measuring contact angle with contact angle goniometer, from side view.

1.1.4 Sliding angle

The contact angle is used as a characterization of the static wettability of a surface, whereas the sliding angle, SA, is a measure of the mobility of a droplet on the surface.
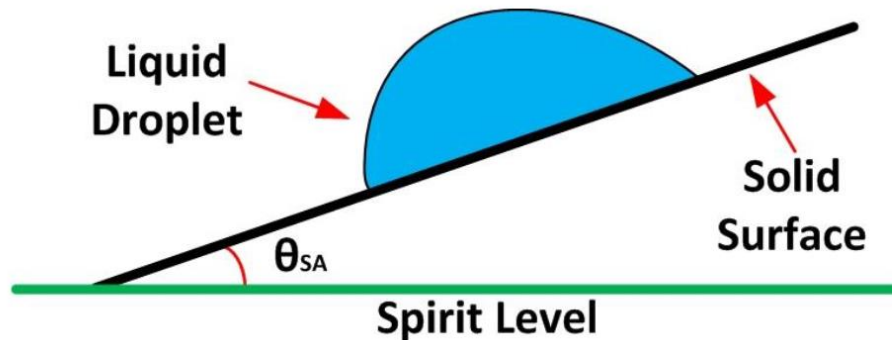
Fig. 1.12 Sliding angle of a surface is defined as the tilted angle of the substrate below when the droplet starts to slide.

Typically, it is defined using the tilted plate goniometry (TPG), where a drop is placed onto a surface. The surface is then inclined and the sliding angle is the tilted angle of

the surface as the droplet begins to slide, as shown in Fig. 1.11[36, 37]. In some literature, sliding angle is also called rolling angle (RA)[38, 39] or tilting angle (TA)[40, 41].

Based on sliding angles, superhydrophobic surfaces can also be divided into low adhesion and high adhesion. Low adhesion superhydrophobic surface refers to a superhydrophobic surface with water sliding angle below 10° [27, 42, 43], such as the Lotus leaf, which is consistent with its self-cleaning property. There are also plants in nature which have a superhydrophobic surface with ultra-high sliding angle, so that water droplets cannot roll off even if the surface is inverted[44, 45]. One of these cases is the petal surface of a red rose, and the phenomena is defined as the 'Petal Effect'[46-48].
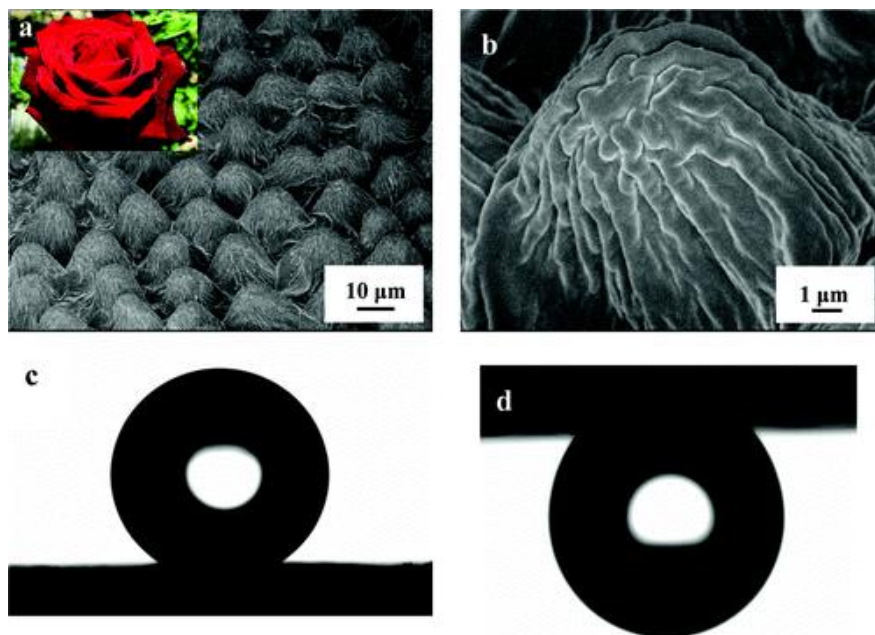
Fig. 1.13 (a, b) SEM images of the surface of a red rose petal, showing a periodic array of micropapillae and nanofolds on each papillae top. (c) Shape of a water droplet on the petal's surface, indicating its superhydrophobicity with a contact angle of 152.4°. (d) Shape of water

on the petal's surface when it is turned upside down. Figures reproduce with permission from Ref. 46.

1.1.5 Contact angle hysteresis

Contact angle hysteresis, or CAH, is another dynamic description of the wettability of the surface.

According to the contact angle models mentioned in last parts, a unique equilibrium contact angle is obtained once a substrate-liquid-vapor system is given. However, in practice we can actually observe a continuous range of value, ranging from the advancing (maximal) contact angle θ_a to the receding (minimal) contact angle θ_r. CAH is defined as the difference between the two[49, 50]:

$$\theta_{CAH} = \theta_a - \theta_r \qquad (1.7)$$

There are two methods that are widely used to measure the advancing and receding contact angles - the tilting-plate goniometry (TPG), as we mentioned above to measure the sliding angle, and captive-drop goniometry (CDG)[51].

The steps of tilting-plate goniometry are similar - additional advancing and receding angles are recorded on left and right sides of the droplet at sliding angle. It is also the method adopted throughout this thesis. In some special cases like the rose petal mentioned in sliding angle part, the liquid droplet does not leave the surface even when the surface is turned upside down, here the advancing and receding contact angles are measured when the surface is tilted at 90°.

In addition, due to the relationship between the advancing contact angle, the receding contact angle and the sliding angle in the tilting-plate scheme, a quantitative expression was derived to describe the relationship[52]:

$$\sin \theta_{SA} = \gamma \frac{Rk}{mg} (\cos \theta_r - \cos \theta_a) \qquad (1.8)$$

where mg is the gravitational force on the droplet of mass m, γ is surface tension, R is the radius and k is a shape constant of the droplet. Usually k is obtained as a fitting parameter based on the experimental data. The components of gravitational force (including friction) and surface tension which act parallel to the surface should have a sum of 0 upon sliding, as shown in Fig. 1.13.
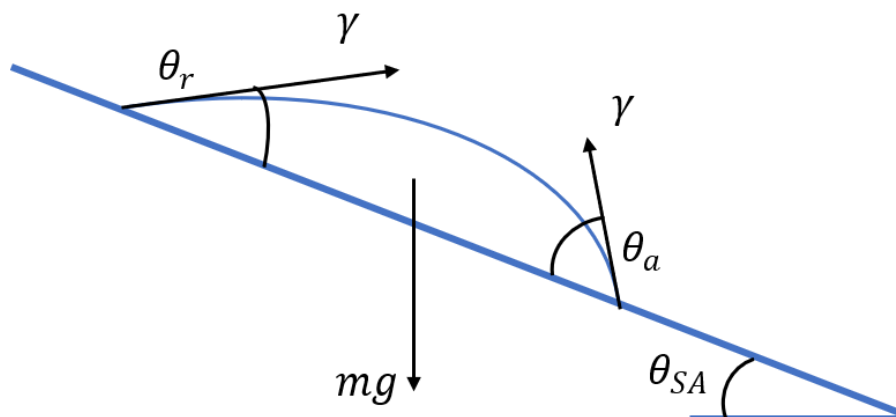
Fig. 1.14 Demonstration of advancing and receding contact angles (θ_a, θ_r), surface tension (γ) and gravitational force (mg) for a droplet on a surface tilted at sliding angle (θ_{SA}).

During the captive-drop goniometry method, advancing contact angle is considered and detected as the largest contact angle possible when adding volume slowly into a droplet on the surface before increasing the solid-liquid contact area. On the

contrary, volume is removed from the droplet to find the smallest possible contact angle without moving the contact line, which is the receding contact angle.
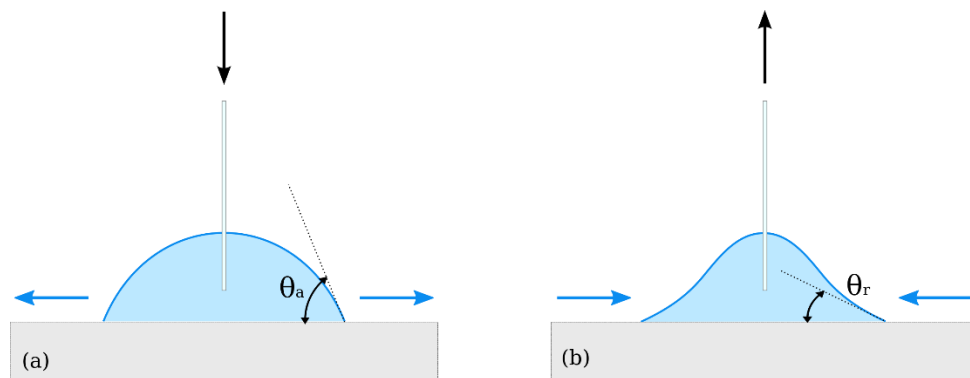
Fig. 1.15 Schemes of the captive-drop goniometry when measuring (a) the advancing contact angle and (b) the receding contact angle.

1.2 Superhydrophobic surfaces

By definition, superhydrophobic surfaces refer to surfaces with water contact angles greater than 150° as discussed previously. Researchers have been inspired by the ultra-water-repellent surfaces in nature, such as Lotus leaves, to do biomimicry and fabricate artificial superhydrophobic surfaces. It has been revealed that the superhydrophobicity of lotus leaves comes from the combination of micrometer-sized papillae and nanometer-sized branchlike protrusions, as well as a layer of superimposed hydrophobic wax covering the papillae. Therefore, the key to synthesis of a superhydrophobic surface is dual-scale roughness and an intrinsic low surface energy material[53].

To achieve the requirement of 'dual-scale roughness and low surface energy', two main routines can be employed to make superhydrophobic surfaces.

One is making a rough surface from a low surface energy material. For example, to roughen fluorinated polymers, silicones, or inorganic TiO_2/ZnO/CuO surfaces with nanorods[53].

The other is to modify a highly-textured surface with a low energy material. Most of these methods are one-step processes and have the advantage of simplicity. But they are always limited to a small set of materials. Specific methods include chemical vapor deposition (CVD), laser/plasma/chemical etching and lithography, sol–gel processing, electrical deposition, etc[53].
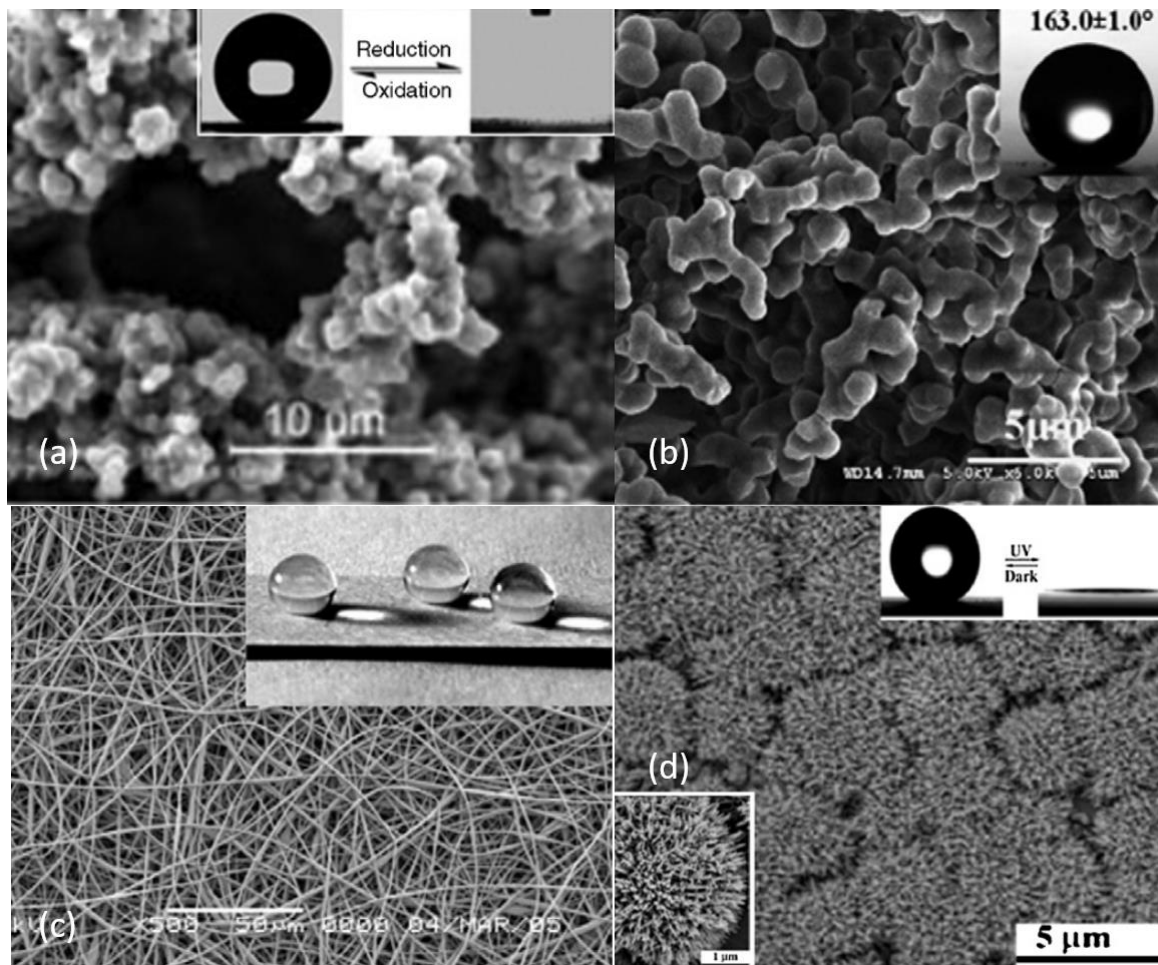
Fig. 1.16 SEM images of superhydrophobic surfaces by roughening low surface energy materials. (a) Roughening a fluorinated material (PPy film)[54]. (b) PS-PDMS surface modified by dimethylformamide (DMF) in humid air[55]. (c) PS-PDMS/PS electrospun fiber mat[56]. (d) TiO$_2$ nanorod film[57]. Figures reproduce with permission.
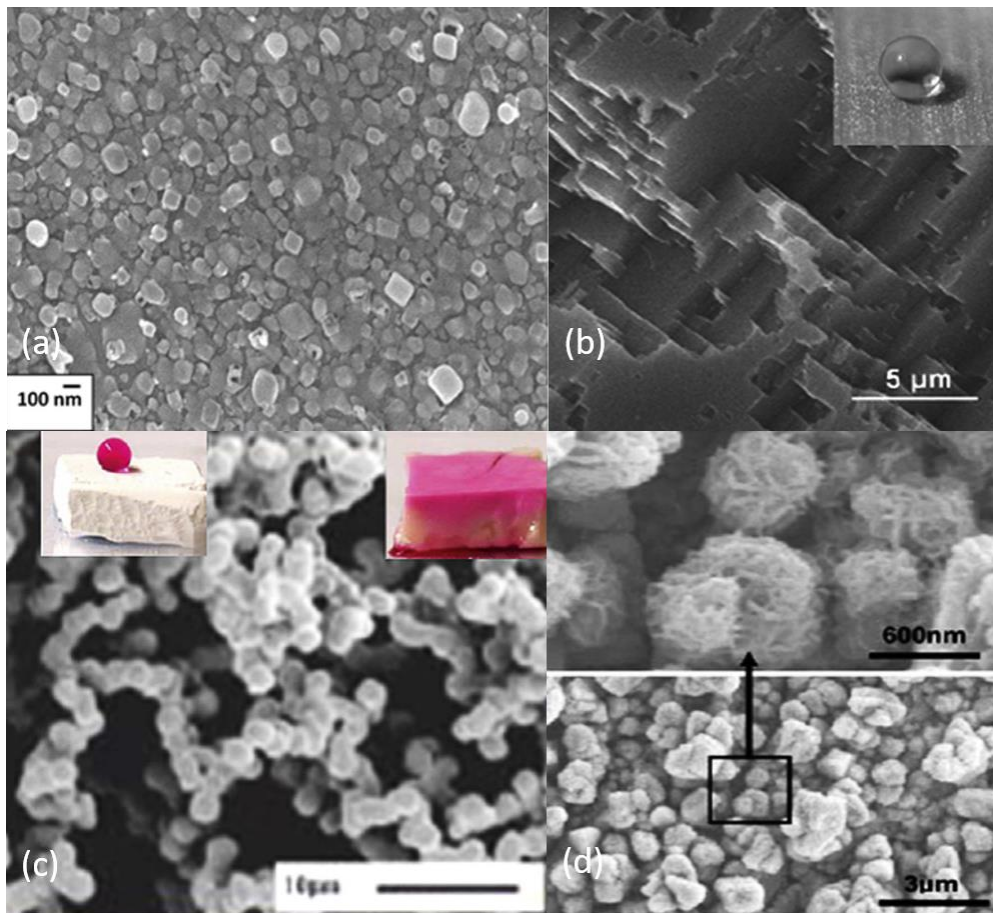
Fig. 1.17 SEM images of superhydrophobic surfaces by modifying a rough surface with low surface energy materials. (a) Superhydrophobic silica coating using AACVD of alkoxysilanes[58]. (b) aluminium surfaces etched with a Beck's dislocation etchant[59]. (c) SEM image of the methyltriethoxysilane (MTEOS) sol–gel foam[60]. (d) The copper surface after electrochemical reaction with sulphur gas[61]. Figures reproduce with permission.

1.2.2 Application of superhydrophobic surfaces

The most intuitive application of superhydrophobic surfaces should be waterproof coatings. Normally a superhydrophobic surface will have the self-cleaning properties, which can be employed on fabrics or covers of electric devices, where dryness is required and water stain should be avoided. In fact, in addition to those water-

repellent and self-cleaning utilities, there are some further applications based on low surface adhesion, such as oil-water separation, anti-icing and anti-bacteria.

As the water-repellent and self-cleaning effect of a superhydrophobic surface is based on the high surface tension of water, those properties do not work with organic solvents, such as peanut oil and hexadecane[62-64]. In other words, the surface can be easily wetted by oil while not by water. Due to this difference, superhydrophobic coatings can be applied to mesh, sponge or membrane to separate water and oil, as the oil part will be able to pass through while the water part will stop at the surface[65, 66]. The oil-water separation properties of superhydrophobic surfaces have great potential to be used for waste water treatment and oil recycling[67].
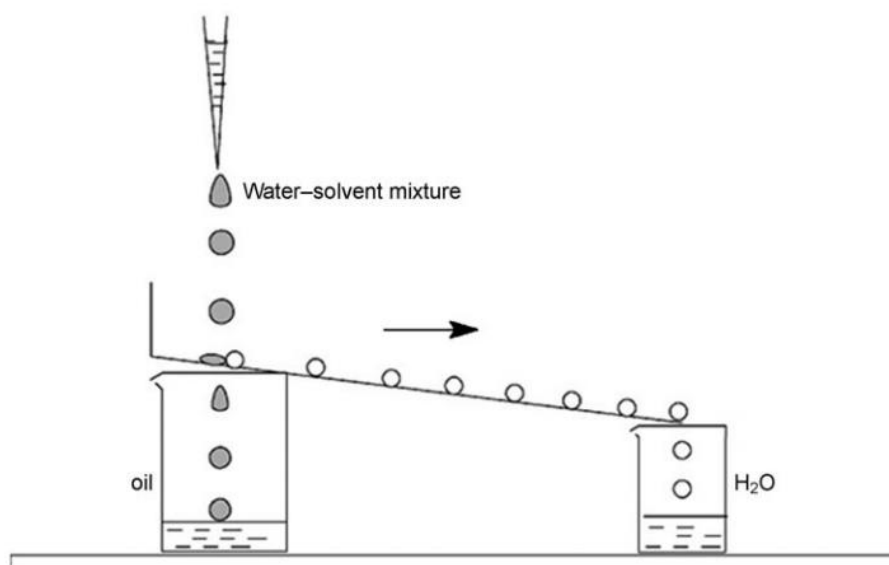
Fig. 1.18 Scheme of oil-water separation with a superhydrophobic copper mesh. Figures reproduce with permission from Ref. 68.

Due to low water adhesion, it has been reported that superhydrophobic surfaces can also be used to repel ice or reduce ice accumulation in low-temperature regions[69, 70].

However, the technique is still in development. Not all superhydrophobic surfaces are icephobic, and even an icephobic surface cannot completely prevent the icing process but delay the ice formation[71]. Also, the ice formed on the surface will increase the adhesion and may even damage the structure[72].

The anti-bacteria function of superhydrophobic surfaces is similar to the self-cleaning effect: due to low adhesion, some of the bacteria may find it difficult to stay on the 'slippery' surface[73] or be cleaned off by rinsing water[74, 75]. This could be enhanced if combining photocatalytic degradation of bacteria, by adding some dye or nanoparticles.

1.3 Summary

The introduction part briefly introduces the phenomena and theories of wetting, as a basis of superhydrophobic surfaces. The Lotus plant was found in nature as an example of non-wetting surface and self-cleaning effect. The microstructure was researched by people and considered as a key factor behind low water adhesion. Researchers then started simple biomimicry to develop advanced fabrication methods and applications of superhydrophobic surfaces.

In the next chapter, a surfactant- and template-free synthesis of superhydrophobic thin films is reported. The approach is based on the growth of Co_3O_4 nanoarchitectures and modification with stearic acid. The surface morphology was found to evolve on a time-dependent basis. After that, the relationships between the water contact angle, sliding angle, water droplet size, and surface microstructures were investigated. A theoretical explanation was provided for the difference in sliding angle and wetting modes on different microstructure surfaces.

In chapter 3, the evaporation of sessile water droplets was explored at different static water contact angles on hydrophobic and superhydrophobic substrates. With the assumption that two evaporation modes, constant contact radius (CCR) mode and constant contact angle (CCA) mode dominate successively during the process the lifetime of the droplets was analyzed with substrate temperature. An evaporative cooling effect was taken into consideration and shown to have a minor influence on the process.

Chapter 4 demonstrates the study on the coalescence and rebound process of binary droplets with different temperatures on superhydrophobic surface. A droplet was set on a superhydrophobic surface while another was released from above to make a head-on collision. By changing the temperature of the incoming droplet, several findings were obtained on the coalescence process and energy conversion. The results may help when hot droplets adhere to solid surfaces in industrial process.

This thesis presents a novel synthesis method to make superhydrophobic surfaces with controllable morphology and performs studies on both static and dynamic interactions between water droplets and superhydrophobic surfaces.

1.4 References

1.   Sumner, A.L., Menke, E.J., Dubowski, Y., Newberg, J.T., Penner, R.M., Hemminger, J.C., Wingen, L.M., Brauers, T. and Finlayson-Pitts, B.J., 2004. The nature of water on surfaces of laboratory systems and implications for heterogeneous chemistry in the troposphere. *Physical Chemistry Chemical Physics*, *6*(3), pp.604-613.

2.   Barthlott, W. and Neinhuis, C., 1997. Purity of the sacred lotus, or escape from contamination in biological surfaces. *Planta*, *202*(1), pp.1-8.

3.   Patankar, N.A., 2004. Mimicking the lotus effect: influence of double roughness structures and slender pillars. *Langmuir*, *20*(19), pp.8209-8213.

4.   Bhushan, B., Jung, Y.C. and Koch, K., 2009. Micro-, nano-and hierarchical structures for superhydrophobicity, self-cleaning and low adhesion. *Philosophical Transactions of the Royal Society A: Mathematical, Physical and Engineering Sciences*, *367*(1894), pp.1631-1672.

5.   Li, X.M., Reinhoudt, D. and Crego-Calama, M., 2007. What do we need for a superhydrophobic surface? A review on the recent progress in the preparation of superhydrophobic surfaces. *Chemical Society Reviews*, *36*(8), pp.1350-1368.

6.   Su, Y., Ji, B., Zhang, K., Gao, H., Huang, Y. and Hwang, K., 2010. Nano to micro structural hierarchy is crucial for stable superhydrophobic and water-repellent surfaces. *Langmuir*, *26*(7), pp.4984-4989.

7.   Cheng, Y.T., Rodak, D.E., Wong, C.A. and Hayden, C.A., 2006. Effects of micro and nano-structures on the self-cleaning behaviour of lotus leaves. *Nanotechnology*, *17*(5), p.1359.

8.   Fürstner, R., Barthlott, W., Neinhuis, C. and Walzel, P., 2005. Wetting and self-cleaning properties of artificial superhydrophobic surfaces. *Langmuir*, *21*(3), pp.956-961.

9.   Chen, X., Wang, C., Chen, J., Onivogui, G. and Song, Y., 2015. Antibacterial activity of lotus leaves (Nelumbo nucifera) against food-borne pathogens. *American Journal of Biochemistry & Biotechnology*, *11*(1), p.11.

10.   Calvert, J.B., 2007. Surface Tension (physics lecture notes). *University of Denver. http://mysite. du. edu/~ jcalvert/phys/surftens. htm. Retrieved*, pp.09-08.

11.   KRÜSS. 2019. Interfacial tension. [online] Hamburg Germany: KRÜSS GmbH. Available from: https://www.kruss-scientific.com/services/education-theory/glossary/interfacial-tension/ [Accessed 8 September 2019].

12.   Gurney, C., 1949. Surface forces in liquids and solids. *Proceedings of the Physical Society. Section A*, *62*(10), p.639.

13.   Harkins, W.D. and Cheng, Y.C., 1921. THE ORIENTATION OF MOLECULES IN SURFACES. VI. COHESION, ADHESION, TENSILE STRENGTH, TENSILE ENERGY, NEGATIVE SURFACE ENERGY, INTERFACIAL TENSION, AND MOLECULAR ATTRACTION. *Journal of the American Chemical Society*, *43*(1), pp.35-53.

14.   Blossey, R., 2003. Self-cleaning surfaces—virtual realities. *Nature materials*, *2*(5), p.301.

15.   Ibach, H., 2006. *Physics of surfaces and interfaces* (Vol. 12). Berlin: Springer.

16.   Patankar, N.A., 2003. On the modeling of hydrophobic contact angles on rough surfaces. *Langmuir, 19*(4), pp.1249-1253.

17.   Feng, L., Li, S., Li, H., Zhai, J., Song, Y., Jiang, L. and Zhu, D., 2002. Super-hydrophobic surface of aligned polyacrylonitrile nanofibers. *Angewandte Chemie International Edition*, *41*(7), pp.1221-1223.

18.   Feng, X., Feng, L., Jin, M., Zhai, J., Jiang, L. and Zhu, D., 2004. Reversible super-hydrophobicity to super-hydrophilicity transition of aligned ZnO nanorod films. *Journal of the American Chemical Society*, *126*(1), pp.62-63.

19.   Young, T., 1805. III. An essay on the cohesion of fluids. *Philosophical transactions of the royal society of London*, (95), pp.65-87.

20.   Wenzel, R.N., 1936. Resistance of solid surfaces to wetting by water. *Industrial & Engineering Chemistry*, *28*(8), pp.988-994.

21.   Wenzel, R.N., 1949. Surface roughness and contact angle. *The Journal of Physical Chemistry*, *53*(9), pp.1466-1467.

22.   Cassie, A.B.D. and Baxter, S., 1944. Wettability of porous surfaces. *Transactions of the Faraday society*, *40*, pp.546-551.

23.   Cassie, A.B.D., 1948. Contact angles. *Discussions of the Faraday society*, *3*, pp.11-16.

24.   Ma, Y., Cao, X., Feng, X., Ma, Y. and Zou, H., 2007. Fabrication of super-hydrophobic film from PMMA with intrinsic water contact angle below 90. *Polymer*, *48*(26), pp.7455-7460.

25.   Yuan, Y. and Lee, T.R., 2013. Contact angle and wetting properties. In Surface science techniques (pp. 3-34). Springer, Berlin, Heidelberg.

26.   Antonini, C., Villa, F., Bernagozzi, I., Amirfazli, A. and Marengo, M., 2013. Drop rebound after impact: The role of the receding contact angle. *Langmuir*, *29*(52), pp.16045-16050.

27.   Miwa, M., Nakajima, A., Fujishima, A., Hashimoto, K. and Watanabe, T., 2000. Effects of the surface roughness on sliding angles of water droplets on superhydrophobic surfaces. *Langmuir*, *16*(13), pp.5754-5760.

28.   Yan, Y.Y., Gao, N. and Barthlott, W., 2011. Mimicking natural superhydrophobic surfaces and grasping the wetting process: A review on recent progress in preparing superhydrophobic surfaces. *Advances in colloid and interface science*, *169*(2), pp.80-105.

29.   Verho, T., Bower, C., Andrew, P., Franssila, S., Ikkala, O. and Ras, R.H., 2011. Mechanically durable superhydrophobic surfaces. *Advanced materials*, *23*(5), pp.673-678.

30.   Yue, Y., Chen, S., Wang, Z., Yang, X., Peng, Y., Cai, J. and Nasr-El-Din, H.A., 2018. Improving wellbore stability of shale by adjusting its wettability. *Journal of Petroleum Science and Engineering*, *161*, pp.692-702.

31.   Lu, Y., Sathasivam, S., Song, J., Crick, C.R., Carmalt, C.J. and Parkin, I.P., 2015. Robust self-cleaning surfaces that function when exposed to either air or oil. *Science*, *347*(6226), pp.1132-1135.

32.   Parkin, I.P. and Palgrave, R.G., 2005. Self-cleaning coatings. *Journal of materials chemistry*, *15*(17), pp.1689-1695.

33.   Shiu, J.Y., Kuo, C.W., Chen, P. and Mou, C.Y., 2004. Fabrication of tunable superhydrophobic surfaces by nanosphere lithography. *Chemistry of materials*, *16*(4), pp.561-564.

34.   Kwok, D.Y., Gietzelt, T., Grundke, K., Jacobasch, H.J. and Neumann, A.W., 1997. Contact angle measurements and contact angle interpretation. 1. Contact angle measurements by axisymmetric drop shape analysis and a goniometer sessile drop technique. *Langmuir*, *13*(10), pp.2880-2894.

35.   Kandlikar, S.G. and Steinke, M.E., 2002. Contact angles and interface behavior during rapid evaporation of liquid on a heated surface. *International Journal of Heat and Mass Transfer*, *45*(18), pp.3771-3780.

36.   Nakajima, A., Abe, K., Hashimoto, K. and Watanabe, T., 2000. Preparation of hard super-hydrophobic films with visible light transmission. *Thin Solid Films*, *376*(1-2), pp.140-143.

37.   Pierce, E., Carmona, F.J. and Amirfazli, A., 2008. Understanding of sliding and contact angle results in tilted plate experiments. *Colloids and Surfaces A: Physicochemical and Engineering Aspects*, *323*(1-3), pp.73-82.

38.   Han, D. and Steckl, A.J., 2009. Superhydrophobic and oleophobic fibers by coaxial electrospinning. *Langmuir*, *25*(16), pp.9454-9462.

39.   Wang, M.F., Raghunathan, N. and Ziaie, B., 2007. A nonlithographic top-down electrochemical approach for creating hierarchical (micro− nano) superhydrophobic silicon surfaces. *Langmuir*, *23*(5), pp.2300-2303.

40.   Koch, K., Bhushan, B., Jung, Y.C. and Barthlott, W., 2009. Fabrication of artificial Lotus leaves and significance of hierarchical structure for superhydrophobicity and low adhesion. *Soft Matter*, *5*(7), pp.1386-1393.

41.	Ming, W., Wu, D., van Benthem, R.A.T.M. and De With, G., 2005. Superhydrophobic films from raspberry-like particles. *Nano letters*, *5*(11), pp.2298-2301.

42.	Zhang, X., Shi, F., Niu, J., Jiang, Y. and Wang, Z., 2008. Superhydrophobic surfaces: from structural control to functional application. *Journal of Materials Chemistry*, *18*(6), pp.621-633.

43.	Guo, Z.G., Liu, W.M. and Su, B.L., 2008. A stable lotus-leaf-like water-repellent copper. *Applied physics letters*, *92*(6), p.063104.

44.	Jin, M., Feng, X., Feng, L., Sun, T., Zhai, J., Li, T. and Jiang, L., 2005. Superhydrophobic aligned polystyrene nanotube films with high adhesive force. *Advanced Materials*, *17*(16), pp.1977-1981.

45.	Bhushan, B. and Her, E.K., 2010. Fabrication of superhydrophobic surfaces with high and low adhesion inspired from rose petal. *Langmuir*, *26*(11), pp.8207-8217.

46.	Feng, L., Zhang, Y., Xi, J., Zhu, Y., Wang, N., Xia, F. and Jiang, L., 2008. Petal effect: a superhydrophobic state with high adhesive force. *Langmuir*, *24*(8), pp.4114-4119.

47.	Bormashenko, E., Stein, T., Pogreb, R. and Aurbach, D., 2009. "Petal effect" on surfaces based on lycopodium: high-stick surfaces demonstrating high apparent contact angles. *The Journal of Physical Chemistry C*, *113*(14), pp.5568-5572.

48.	Ebert, D. and Bhushan, B., 2012. Wear-resistant rose petal-effect surfaces with superhydrophobicity and high droplet adhesion using hydrophobic and hydrophilic nanoparticles. *Journal of colloid and interface science, 384*(1), pp.182-188.

49.	Extrand, C.W. and Kumagai, Y., 1997. An experimental study of contact angle hysteresis. *Journal of Colloid and interface Science*, *191*(2), pp.378-383.

50.	Ouchi, T., Kontani, T., Saito, T. and Ohya, Y., 2005. Suppression of cell attachment and protein adsorption onto amphiphilic polylactide-grafted dextran films. *Journal of Biomaterials Science, Polymer Edition*, *16*(8), pp.1035-1045.

51.   Krishnan, A., Liu, Y.H., Cha, P., Woodward, R., Allara, D. and Vogler, E.A., 2005. An evaluation of methods for contact angle measurement. *Colloids and Surfaces B: Biointerfaces*, *43*(2), pp.95-98.

52.   Pierce, E., Carmona, F.J. and Amirfazli, A., 2008. Understanding of sliding and contact angle results in tilted plate experiments. *Colloids and Surfaces A: Physicochemical and Engineering Aspects*, *323*(1-3), pp.73-82.

53.   Ma, M. and Hill, R.M., 2006. Superhydrophobic surfaces. *Current opinion in colloid & interface science*, *11*(4), pp.193-202.

54.   Xu, L., Chen, W., Mulchandani, A. and Yan, Y., 2005. Reversible conversion of conducting polymer films from superhydrophobic to superhydrophilic. *Angewandte Chemie International Edition*, *44*(37), pp.6009-6012.

55.   Zhao, N., Xie, Q., Weng, L., Wang, S., Zhang, X. and Xu, J., 2005. Superhydrophobic surface from vapor-induced phase separation of copolymer micellar solution. *Macromolecules*, *38*(22), pp.8996-8999.

56.   Ma, M., Hill, R.M., Lowery, J.L., Fridrikh, S.V. and Rutledge, G.C., 2005. Electrospun poly (styrene-block-dimethylsiloxane) block copolymer fibers exhibiting superhydrophobicity. *Langmuir*, *21*(12), pp.5549-5554.

57.   Feng, X., Zhai, J. and Jiang, L., 2005. The fabrication and switchable superhydrophobicity of TiO2 nanorod films. *Angewandte Chemie International Edition*, *44*(32), pp.5115-5118.

58.   Tombesi, A., Li, S., Sathasivam, S., Page, K., Heale, F.L., Pettinari, C., Carmalt, C.J. and Parkin, I.P., 2019. Aerosol-assisted chemical vapour deposition of transparent superhydrophobic film by using mixed functional alkoxysilanes. *Scientific reports*, *9*(1), p.7549.

59.   Qian, B. and Shen, Z., 2005. Fabrication of superhydrophobic surfaces by dislocation-selective chemical etching on aluminum, copper, and zinc substrates. *Langmuir*, *21*(20), pp.9007-9009.

60.   Shirtcliffe, N.J., McHale, G., Newton, M.I., Perry, C.C. and Roach, P., 2005. Porous materials show superhydrophobic to superhydrophilic switching. *Chemical Communications*, (25), pp.3135-3137.

61.   Han, J.T., Jang, Y., Lee, D.Y., Park, J.H., Song, S.H., Ban, D.Y. and Cho, K., 2005. Fabrication of a bionic superhydrophobic metal surface by sulfur-induced morphological development. *Journal of Materials Chemistry*, *15*(30), pp.3089-3092.

62.   Yao, X., Gao, J., Song, Y. and Jiang, L., 2011. Superoleophobic surfaces with controllable oil adhesion and their application in oil transportation. *Advanced Functional Materials*, *21*(22), pp.4270-4276.

63.   Darmanin, T. and Guittard, F., 2009. Super oil-repellent surfaces from conductive polymers. *Journal of Materials Chemistry*, *19*(38), pp.7130-7136.

64.   Steele, A., Bayer, I. and Loth, E., 2008. Inherently superoleophobic nanocomposite coatings by spray atomization. *Nano letters*, *9*(1), pp.501-505.

65.   Wang, C.F. and Lin, S.J., 2013. Robust superhydrophobic/superoleophilic sponge for effective continuous absorption and expulsion of oil pollutants from water. *ACS applied materials & interfaces*, *5*(18), pp.8861-8864.

66.   Wu, L., Zhang, J., Li, B. and Wang, A., 2014. Mechanical-and oil-durable superhydrophobic polyester materials for selective oil absorption and oil/water separation. *Journal of colloid and interface science*, *413*, pp.112-117.

67.   Song, J., Huang, S., Lu, Y., Bu, X., Mates, J.E., Ghosh, A., Ganguly, R., Carmalt, C.J., Parkin, I.P., Xu, W. and Megaridis, C.M., 2014. Self-driven one-step oil removal from oil spill on water via selective-wettability steel mesh. *ACS applied materials & interfaces*, *6*(22), pp.19858-19865.

68.   Crick, C.R. and Parkin, I.P., 2010. Preparation and characterisation of super-hydrophobic surfaces. *Chemistry–A European Journal*, *16*(12), pp.3568-3588.

69.   Frankenstein, S. and Tuthill, A.M., 2002. Ice adhesion to locks and dams: past work; future directions? *Journal of Cold Regions Engineering*, *16*(2), pp.83-96.

70.   Parent, O. and Ilinca, A., 2011. Anti-icing and de-icing techniques for wind turbines: Critical review. *Cold regions science and technology*, *65*(1), pp.88-96.

71.   Cao, L., Jones, A.K., Sikka, V.K., Wu, J. and Gao, D., 2009. Anti-icing superhydrophobic coatings. *Langmuir*, *25*(21), pp.12444-12448.

72.   Farhadi, S., Farzaneh, M. and Kulinich, S.A., 2011. Anti-icing performance of superhydrophobic surfaces. *Applied Surface Science*, *257*(14), pp.6264-6269.

73.   Zhang, X., Wang, L. and Levänen, E., 2013. Superhydrophobic surfaces for the reduction of bacterial adhesion. *Rsc Advances*, *3*(30), pp.12003-12020.

74.   Privett, B.J., Youn, J., Hong, S.A., Lee, J., Han, J., Shin, J.H. and Schoenfisch, M.H., 2011. Antibacterial fluorinated silica colloid superhydrophobic surfaces. *Langmuir*, *27*(15), pp.9597-9601.

75.   Crick, C.R., Ismail, S., Pratten, J. and Parkin, I.P., 2011. An investigation into bacterial attachment to an elastomeric superhydrophobic surface prepared via aerosol assisted deposition. *Thin Solid Films*, *519*(11), pp.3722-3727.

76.   Crick, C.R., Bear, J.C., Kafizas, A. and Parkin, I.P., 2012. Superhydrophobic photocatalytic surfaces through direct incorporation of titania nanoparticles into a polymer matrix by aerosol assisted chemical vapor deposition. *Advanced Materials*, *24*(26), pp.3505-3508.

Chapter 2. Synthesis of superhydrophobic surfaces with Wenzel and Cassie–Baxter state

2.1 Introduction

Two surface states are widely used to describe a superhydrophobic surface: the Cassie–Baxter state and the Wenzel state. During the Cassie–Baxter state water droplets sit on the micro-protrusions and can easily roll across a tilted surface. However, in the Wenzel state, water droplets penetrate the surface porosity and get pinned in place, making the surface look 'sticky'. Transition between Cassie–Baxter and Wenzel state is known but not completely understood[1].

The volume of water droplets may act as an important factor in deciding whether a surface displays Wenzel or Cassie–Baxter type superhydrophobicity[2]. For example, on rain proofing fabrics made by superhydrophobic materials, it is often observed that not all water droplets roll effectively to clean the surface. Droplets below a particular size may stick even when the surface is vertical or upside down, showing a Wenzel type behaviour[3]. It is necessary, therefore, to investigate the relationship between the factors including size of water droplets, the sliding angle, the contact angle, and the microstructure of rough hydrophobic surfaces. There are a number of reports on the rolling and adhesion of water droplets[4-12]. However, a comprehensive understanding of the sliding properties of water droplets with different sizes, especially for small water droplets on superhydrophobic surfaces, has not yet been sufficiently achieved[13-16].

In this chapter, the fabrication of superhydrophobic cobalt oxide (Co_3O_4) films is reported, by combining a simple solution-immersion process and the self-assembly of stearic acid. The microstructure of the Co_3O_4 films shows a time-dependent behaviour and can be tailored from nanowire arrays to nanowire/micro-flower structures, and finally to micro-flowers by adjusting reactions time.

The wetting behaviour (Cassie–Baxter or Wenzel state) of water droplets with different volume and their relationship with surface microstructures is also investigated. The variation of the sliding angle with different droplet volumes fitted well with existing theory.

2.2 Experimental

2.2.1 Preparation of superhydrophobic Co_3O_4 film

The superhydrophobic Co_3O_4 film was generated by an immersion process and a modification by stearic acid. Following is the detailed process:

1. 5 mmol of cobalt nitrate hexahydrate ($Co(NO_3)_2 \cdot 6H_2O$) and 15 mmol of urea ($CO(NH_2)_2$) were dissolved in 50 mL of distilled water to form a homogeneous solution.

2. A piece of clean aluminium sheet (10 × 30 × 1 mm) was immersed in the reaction solution and maintained at 97 °C for a certain time.

3. The sample was taken out and rinsed with distilled water several times in order to remove the free particle debris and the residual reactant.

4. The sample was annealed at 250 °C in air for 2 h leading to the formation of Co_3O_4 film with controlled morphology.

5. The annealed sample was immersed in 0.015 mol/l of stearic acid in ethanol for 2h, taken out, washed with ethanol, and dried at 85 °C for 1h.
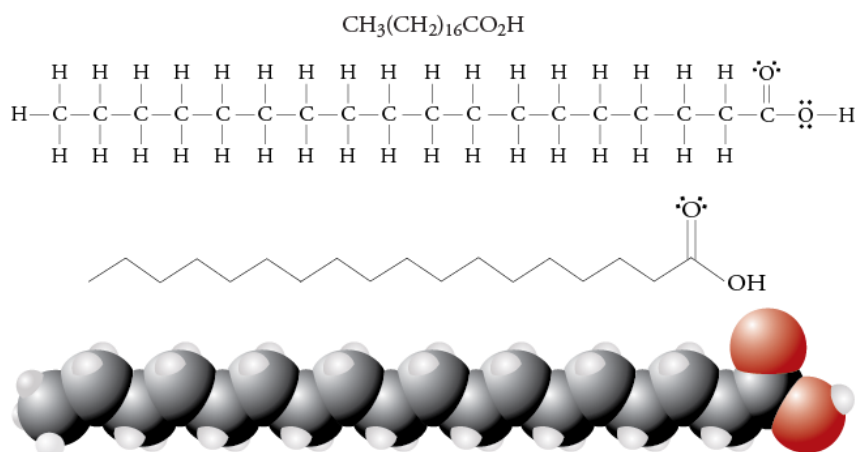
Fig. 2.1 Chemical structure of stearic acid.

2.2.2 Characterization

Surface morphologies and structure

The morphologies and structures of the surfaces were characterized by FESEM (JEOL JSM-6701F FESEM), high-resolution TEM (HRTEM, JEOL JEM-2010F) and XRD (RIGAKU D/Max-2550 with Cu-Kα radiation). XPS data were acquired using a VGESCALAB210 x-ray photoelectron spectrometer.

Contact angles and sliding angles

Water contact angles and sliding angles were measured using a KRÜSS DSA-100 apparatus. The volume of the water droplets in the measurement about 4–6 μL.

Surface adhesion of water droplets

Adhesive action was measured by a highly-sensitive electromechanical balance system. First, the superhydrophobic surface was placed on the plate of the balance system, microdroplets with different volumes were suspended on a metal ring, and the force of the balance system was initialized to zero. Then the surface was brought into contact with the microdroplet while maintaining the balance force at zero. The surface was moved at a rate of 0.05 mm s^{-1}. When the surface left the microdroplet

after contact, the balance force increased gradually and reached its maximum. Finally, the balance force dropped immediately when the surface detached from the microdroplet to finish one cycle of the measurement.

2.3 Results and discussion

2.3.1 Structural characterization and growth of crystalline Co_3O_4 film

As shown in the SEM images (Figures 2.2 (a) and (b)), the sample surface after 13h of immersion time is uniformly and densely covered with nanowires, which are joined together at the top and to form arch-like structures.

The detailed microstructures of the nanowires were further investigated by TEM. As shown in figure 2.2 (c), the nano-branch is composed of 10−15 nm nanocrystals which are packed into a compact linear structure. The selected area electron diffraction (SAED) pattern is also attached as an inset in figure 2.2 (c) and indicates that the nanowires consist of multiple crystallites.

The structure and phase of the sample after annealing at 250 °C for 2 h were determined by XRD analysis (figure 2.2 (d)). All the diffraction peaks are attributed to the spinel Co_3O_4 phase (JCPDS (JCPDS NO: 48-0083) card no. 42-1467) indicating that crystalline Co_3O_4 has been successfully formed after annealing. The cubic spinel phase of Co_3O_4 was found to have a lattice constant of a = 8.084 Å, which is also consistent with the standard XRD pattern for Co_3O_4 (JCPDS card no. 42-1467, a = 8.084 Å). Besides, no impurity peaks were detected by XRD, confirming that the cobalt oxide contained no easily measurable second crystalline phase.
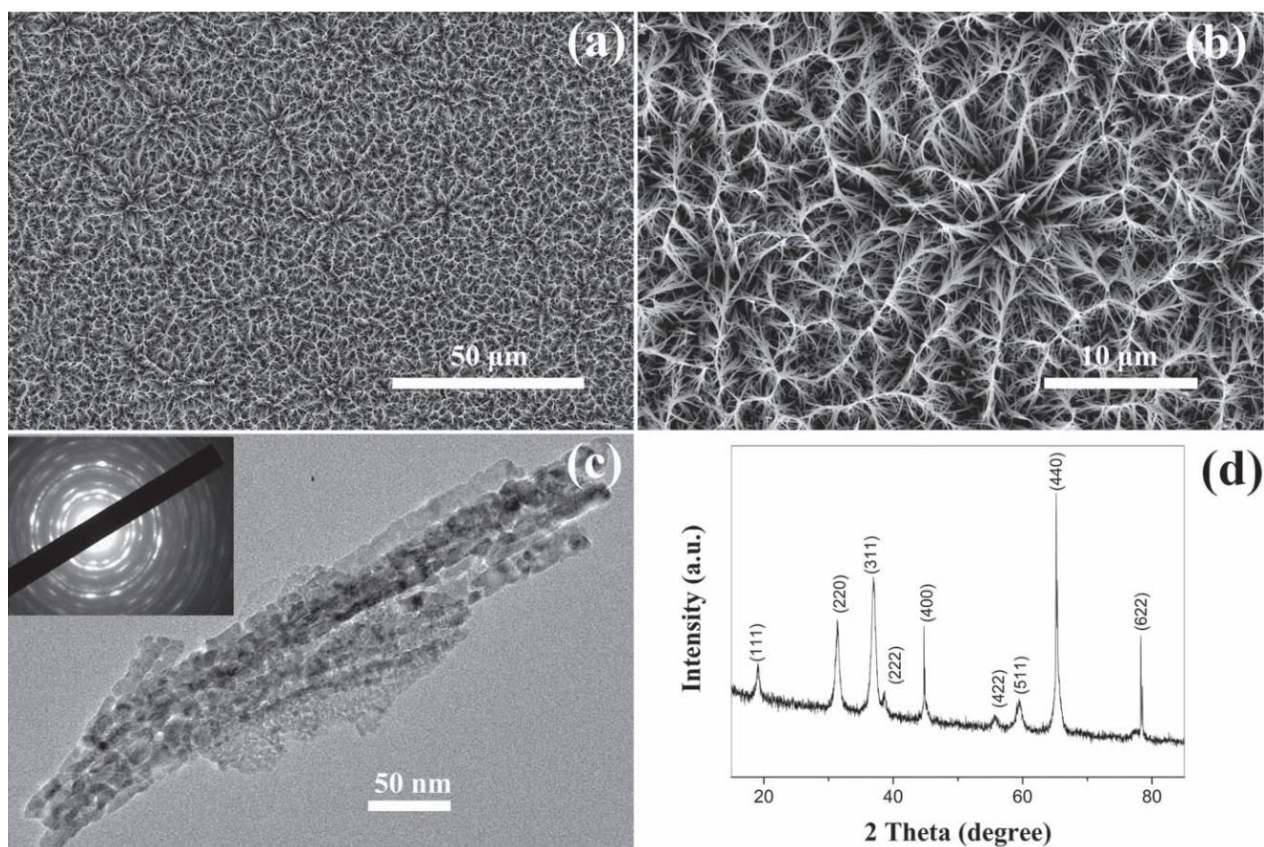
Fig 2.2 Characterization of the of the Co_3O_4 film with 13 h immersion process and after annealing at 250 °C for 2 h. (a), (b) SEM images; (c) TEM image; (d) XRD pattern. Inset in (c) is the corresponding SAED pattern.

The morphology of the Co_3O_4 film was tailored to different microstructures by adjusting the reaction time, shown in figure 2.3. When the immersion time comes to 15 h, it could be observed that some nanosheets grow from the nanowire arrays and this is the initial formation of the micro-flower, as shown in figures 2.3 (a) and (b). An increase in the immersion time leads to an enlarged surface area of the micro-flower structures. Also, the micro-flowers coexist with nanowires on the surface to achieve micro-flower/nanowire array structures. If the immersion time reaches 18 h, the number, size and density of the micro-flowers further increase. The high-resolution SEM image (figure 2.3 (d)) reveals that the structure at this stage is composed of two

parts. The upper part contains micro-flowers and the bottom is made up of original nanowire arrays. The micro-flowers are in fact hierarchical architectures consisting of nanosheets as building units. These 'unit' nanosheets are compacted at the 'root' and extend outside. Finally, an increase in the reaction time to 20 h made the nanowire structure completely covered with micro-flowers with diameters of 8–10 µm, as shown in figures 2.3 (e), (f). Close observation unveils that the hierarchical micro-flowers contain dozens of nano-petals about 0.8–1.5 µm wide and 10–20 nm thick.

By analysing the time-dependent morphology evolution processes, it is believed that the growth of the hierarchical architecture has three general stages: (i) formation and growth of nanowires; (ii) formation and growth of flower-like structures from nanowire arrays; and (iii) further growth of micro-flowers on top of the nanowire array films. The growth process is shown in figure 2.4.

At the initial reaction stage, accompanying the CO_3^{2-} and OH^- anions from hydrolysis of urea reacting with Co^{2+} cations, the initial crystal nucleus of cobalt carbonate hydroxide hydrate starts to come into being[17]. After that, the newly formed nano-nuclei tend to gather together as they are thermodynamically unstable due to high surface energy. As a result, the supersaturated nuclei aggregate together and form nanowire arrays.
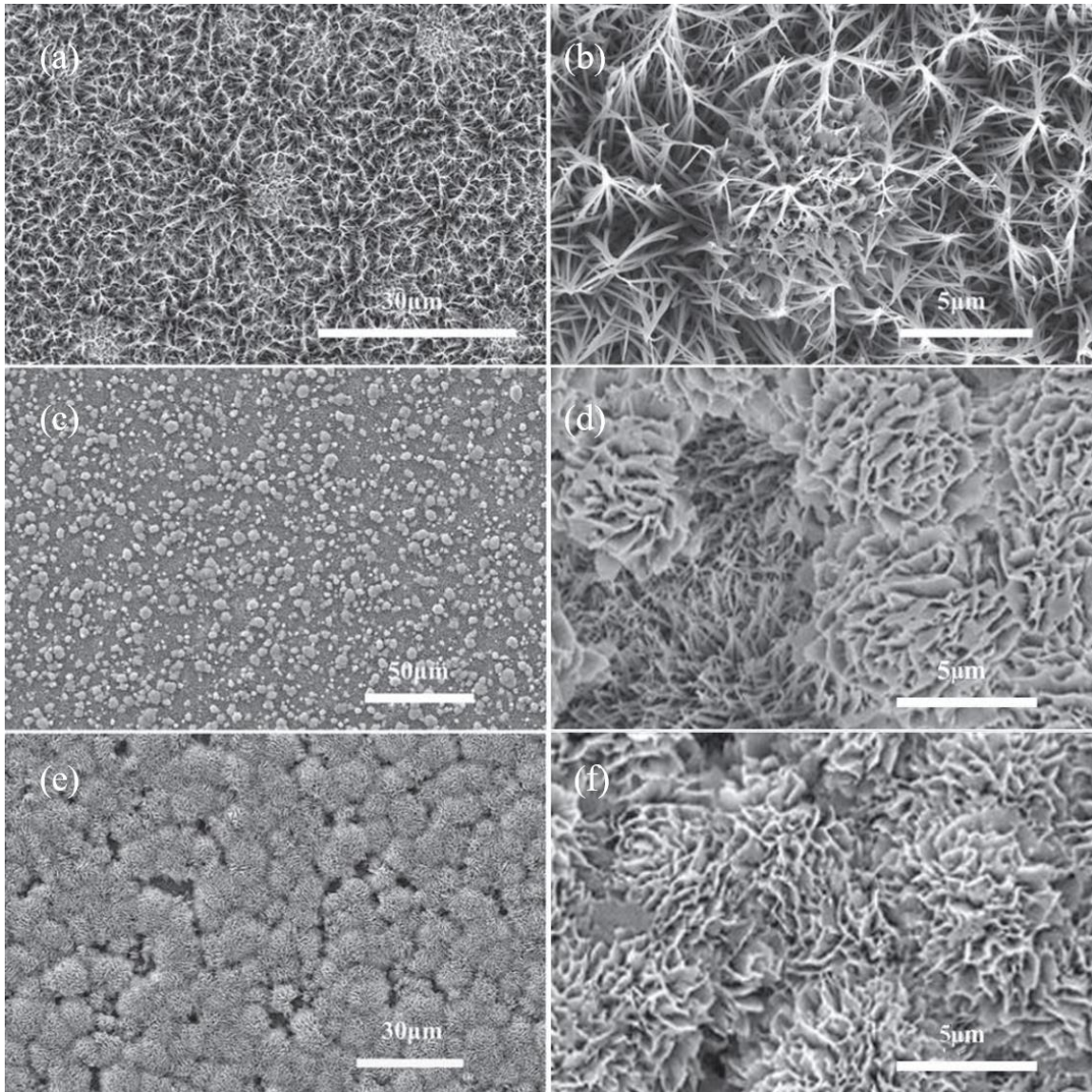
Fig. 2.3 SEM images of the film with different reaction times. (a), (b) 15 h; (c), (d) 18 h; (e), (f) 20 h.
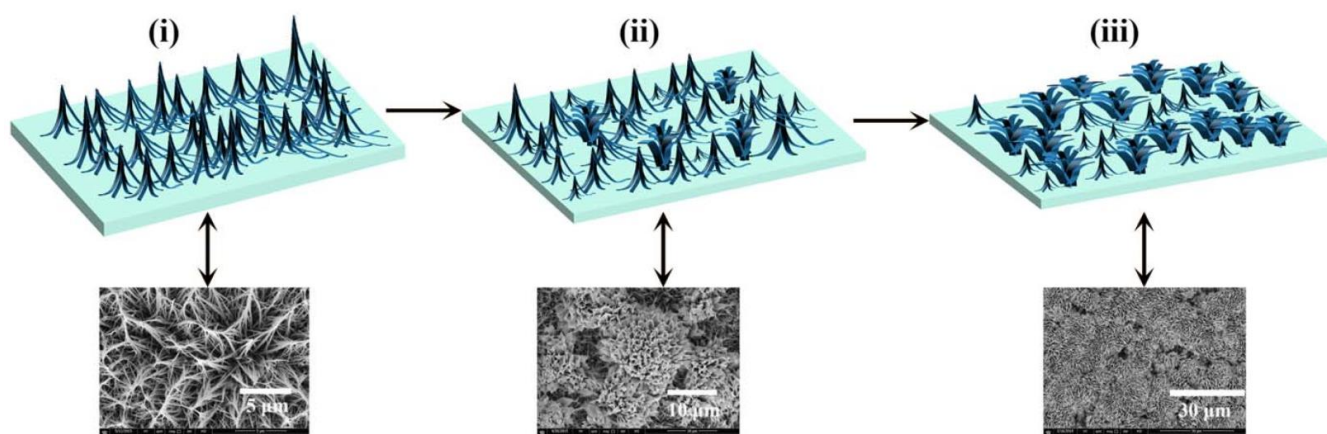
Fig. 2.4 Schematic of the microstructure evolution process of Co_3O_4 film and SEM images corresponding to each growth stage. Parts (i), (ii), and (iii) represent the sample film with reaction time of 13 h, 18 h, and 20 h, respectively.

During subsequent stages, the cobalt carbonate hydroxide hydrate nanowire arrays grow further in length and width into nanosheets which coexist with the nanowires. As the reaction continues, more and more nanosheets are formed, grow larger and construct hierarchical micro-flower architectures by consuming core materials via an Ostwald ripening process. Finally, hierarchical micro-flowers made of nanosheets as building units almost completely cover the nanowire structures. After calcination at each stage, morphologies were found to be unchanged. Hence, it is believed that the cobalt carbonate hydroxide hydrate film transforms into Co_3O_4 film and the microstructures virtually remain the same[18].

In order to further understand the composition and the wettability transition from superhydrophilicity to superhydrophobicity after chemical modification with stearic acid, XPS characterization was adopted. Shown in figure 2.5 (a) is the survey spectrum of the as-prepared Co_3O_4 film before and after chemical modification. Only elements Co, O (and adventitious C) were detected, indicating the surface purity of

the product. Compared with the result before modification with stearic acid, the C

content increases due to the added stearic acid (upper line). Figure 2.5 (b) shows

two peaks at 780.1 eV (Co2p$_{3/2}$) and 795.0 (Co2p$_{1/2}$) with a spin-orbit splitting of 14.9

eV, verifying the formation of Co_3O_4 [19]. The O1s spectrum (figure 2.5 (c)) is modelled

to resolve into multiple components centred at binding energies of 530.5, 531.3, and

532.0 eV, which are ascribed to Co–O, C=O, and −OH species, respectively[20].

Figure 2.5 (d) demonstrates C1s spectrum before and after modification. The carbon

element appearance before the modification is considered to come from the

contamination from the equipment. Clearly, the carbon component increases after

coating with stearic acid (figure 2.5 (d) upper red line), indicating that very thin layers

of stearic acid are attached to the surface of the Co_3O_4 film
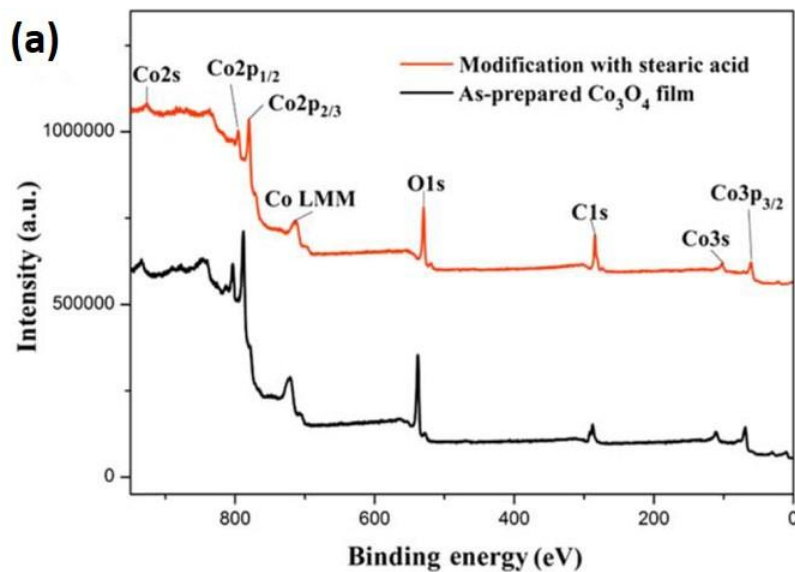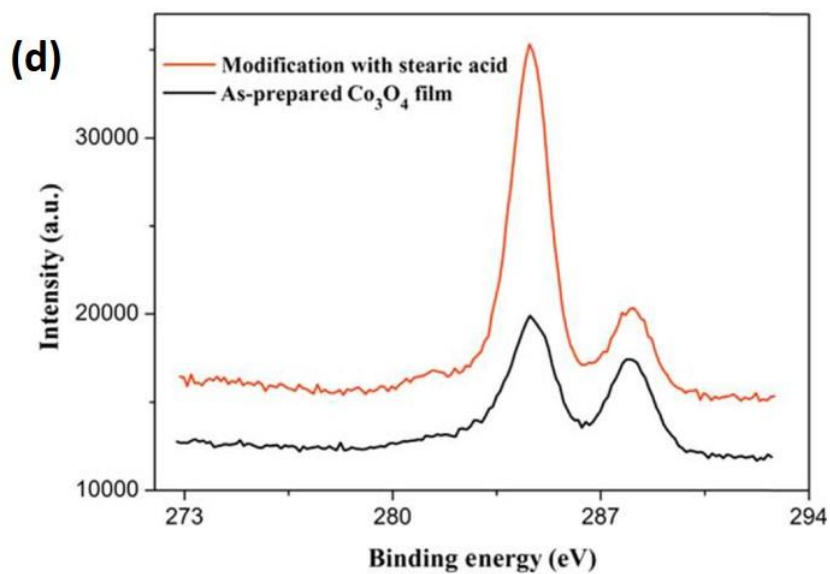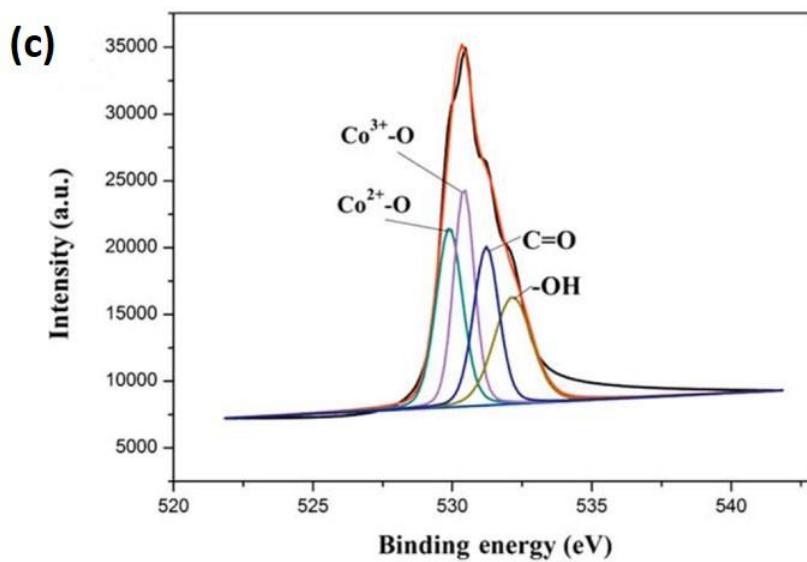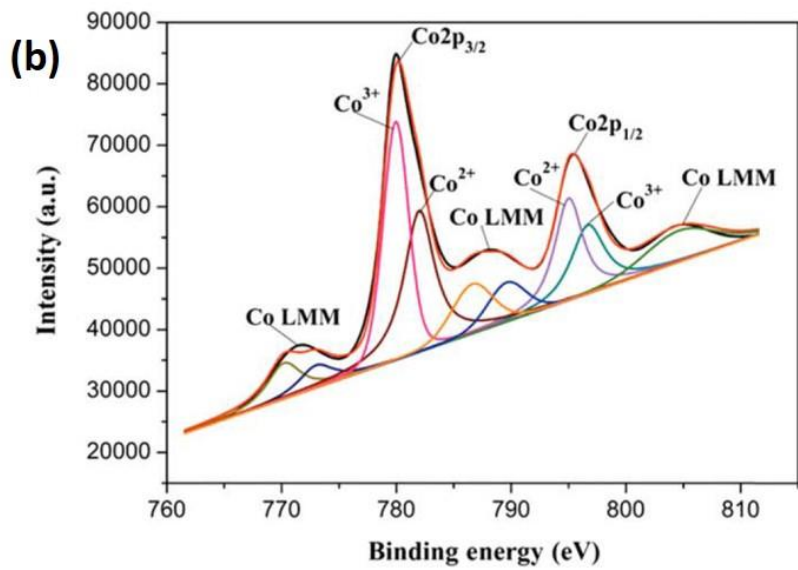
Fig. 2.5 (a) XPS spectra for the obtained film surface before and after stearic acid modification. (b) The spectrum of Co2p. (c) The decomposed spectrum of O1s after stearic acid modification. (d) C1s spectrum before and after surface modification.

2.3.2 Morphology-dependent wetting behaviour

The surfaces demonstrate a transition from a Wenzel to Cassie–Baxter state as droplet volume changes. Herein, the influences of the surface microstructures and water droplet size on the contact angle and sliding angle values are investigated. Figure 2.6 (a) shows the static contact angle values of water droplets of various volumes on different films. The changes in contact angle led by a reduction in droplet volume from 10 µL to 1 µL on the same surface do not exceed the inherent errors of the measurement. Therefore, in the range of this experiment, size of the water droplet is shown not to be a key factor that affects the contact angle at the contact line, which is consistent with those in the literature[18]. However, in our work, it was found that for droplets of equal volume the sliding angle values were markedly different and dependent on the surface morphology. Figure 2.6 (b) shows the relationship between sliding angle values and droplet volume on different micro-structured surfaces. It is clear that the sliding angle values are higher for smaller water drops on surfaces with the same micro-structure. On the nanowire array surface, the sliding angle value decreases from 20 ± 1° to 4 ± 1° as the drop volume increases from 1 µL to 10 µL. With increasing reaction time, the surface microstructure transforms from a nanowire array to coexisting nanowire and micro-flowers, and finally to hierarchical micro-flowers. As shown in figures 2.6 (a) and (b), for a 10 µL water droplet, the static contact angle value will decrease from 164 ± 1° on the nanowire array surface (13 h reaction time) to 158 ± 1° on the micro-flower

structure surface (18 h reaction time), whereas the corresponding sliding angle value

will increase from 4 ± 1° to 15 ± 1°
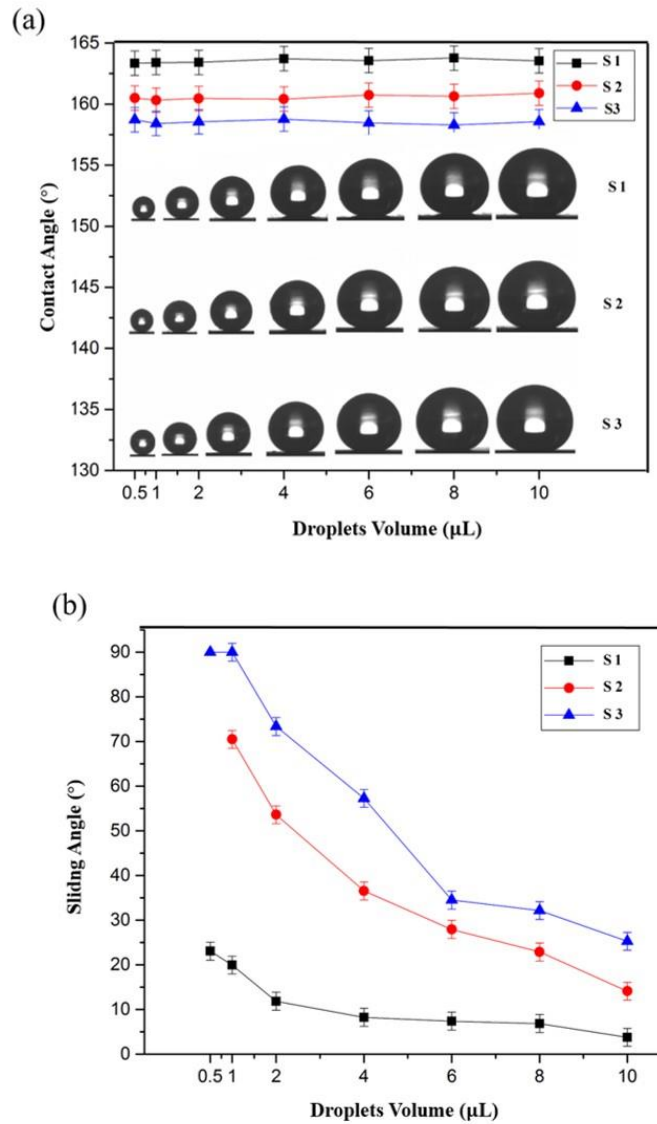
Fig. 2.6 The relationship between contact angle (a) and sliding angle (b) values and droplet

volume on different surfaces with reaction times of 13 h (S1), 16 h (S2), and 18 h (S3). The

volume of droplets inset in (a) from left to right is 0.5, 1, 2, 4, 6, 8, 10 μL.

The adhesive force of different droplets on the superhydrophobic surface with

different microstructures was researched to further investigate the variation of sliding

angle. Figures 2.7 (a)–(c) show force−distance curves on the superhydrophobic surfaces with reaction times of 13 h, 16 h, and 18 h. It can be seen that the adhesive force increases as the droplet volume decreases, or a smaller drop is more likely to be fixed on the surface. Therefore, the sliding angle will also increase as droplet volume decreases.

Surface roughness also plays an important role in the sliding angle of a droplet with a fixed size. As shown in figure 2.7 (d), the adhesive force of a droplet is lower on the nanowire surface than on the micro-flower structure surface, which is consistent with the result that droplets have a smaller sliding angle on the nanowire type surface than on the micro-flower structure surface.
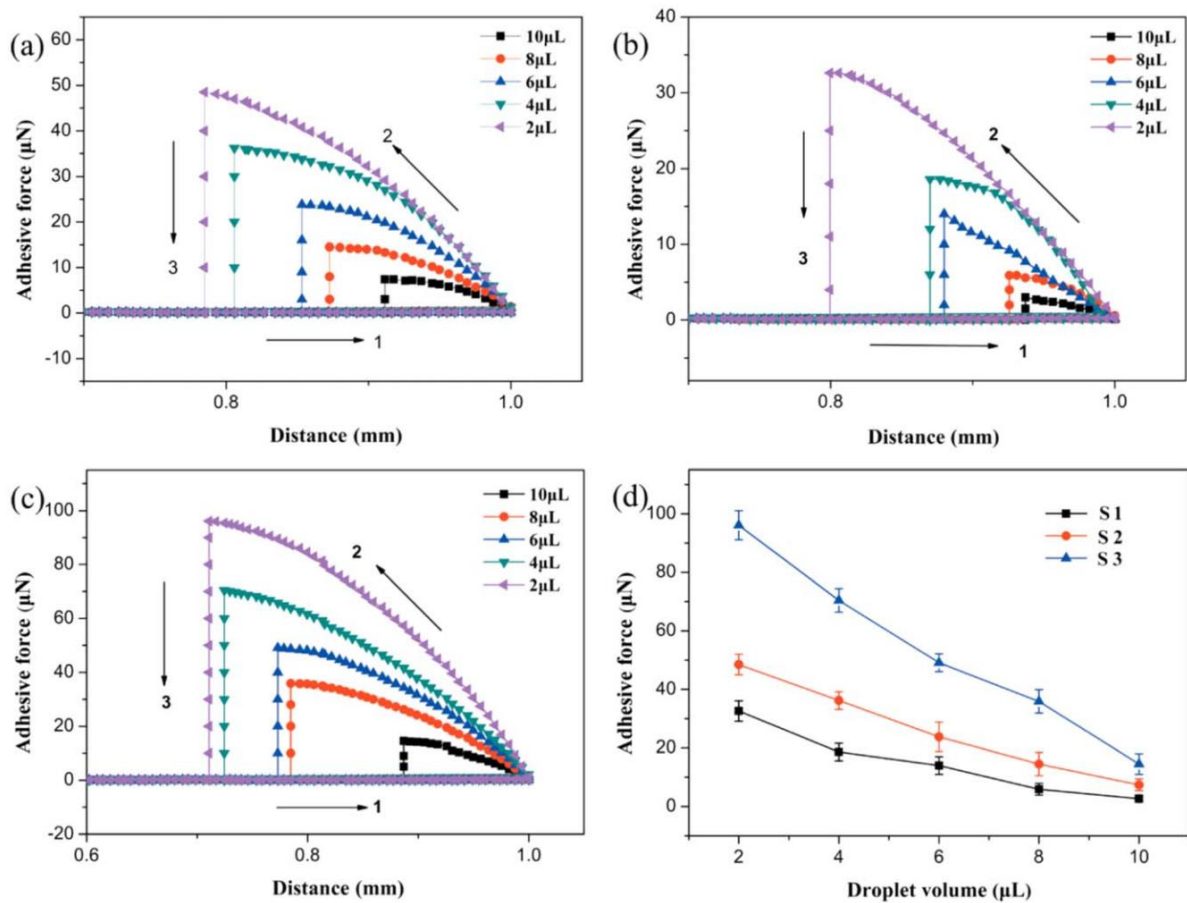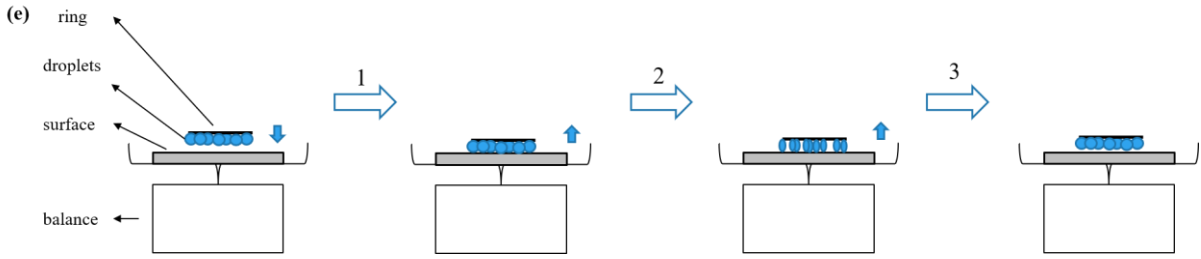
Fig. 2.7 Force−distance curves on the superhydrophobic surfaces under reaction times of 13 h (a), 16 h (b), and 18 h (c). The relationship between the adhesive force and the droplet volume is shown in (d). (e) gives an illustration of the 3 steps.

2.3.3. Theoretical insight into wetting behaviour

Surface roughness is believed to behind the difference in adhesive force and droplets behaviour between the nanowire type and the micro-flower structure surfaces.

Typically, water contact angle has a higher value on a rougher surface, which can be verified with theory.

Young's equation describes the contact angle of a sessile droplet on a smooth solid surface, and Wenzel and Cassie-Baxter models describe that on a rough one[21, 22]:

$$\gamma_{LS} - \gamma_{SV} + \gamma_{LV} \cdot \cos\theta_Y = 0$$

$$\cos\theta_W = r \cdot \cos\theta_Y$$

$$\cos\theta_{CB} = f_s \cdot \cos\theta_s + f_v \cdot \cos\theta_v \qquad (2.1)$$

The droplets during this experiment are smaller than 10µL, which can be treated as spherical cap when placed on the substrate, whose volume is given by

$$V = \frac{\pi R^3 (1 - \cos\theta)^2 (2 + \cos\theta)}{3\sin^3\theta} \qquad (2.2)$$

The contact radius is

$$R = \left(\frac{3\sin^3\theta \cdot V}{\pi(1-\cos\theta)^2(2+\cos\theta)}\right)^{\frac{1}{3}} \qquad (2.3)$$

Masashi Miwa and his co-workers investigated the relationship between contact angles and sliding angles on a rough surface[15]:

$$\sin\alpha = \frac{2Rk\sin\theta(1+\cos\theta)}{g(1+R\cos\theta')}\left[\frac{3\pi^2}{m^2\rho(2-3\cos\theta+\cos^3\theta)}\right]^{1/3} \qquad (2.4)$$

Here θ is and θ' are the contact angles of the rough and flat surfaces. Therefore, droplets on the same substrate would illustrate the relationship

$$\sin\alpha \propto \frac{R}{(1+R\cos\theta')m^{\frac{2}{3}}} \qquad (2.5)$$

For droplets with volume < 10 μL and contact angle > 150°, the contact radius R is of order 10^{-4}m, thus $1 + R\cos\theta' \approx 1$, then (2.5) can be simplified to

$$\sin\alpha \propto \frac{R}{m^{\frac{2}{3}}} \qquad (2.6)$$

The range of contact radius of the droplets used in this experiment is calculated to be 130 μm ≤ R ≤ 490 μm, which is far beyond the scale of the micro-structures shown in Fig. 2.3. Thus, it is considered that the fact that the surface structure transforms from nano-needles and wires to nano-plates and flowers as the immersion times increases slightly lowers the surface roughness and leads to the diminution of sliding angle.
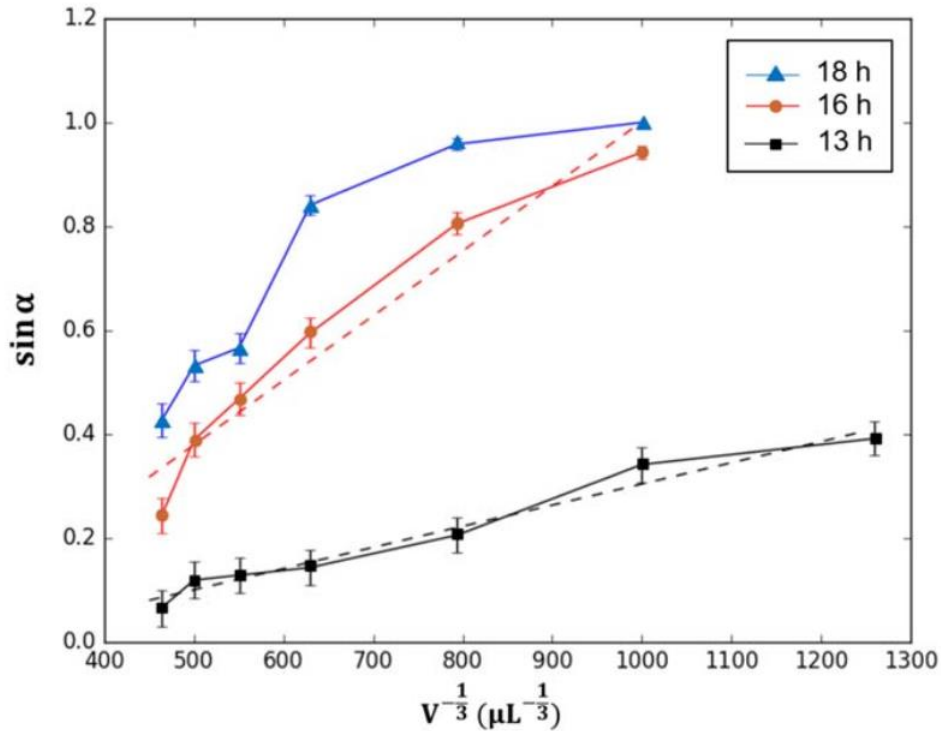
Fig. 2.8 Sine value of the sliding angle plotted against V$^{-1/3}$. ▲, ● and ■ represent actual data points, and the dotted lines plot the theoretical model.

In line with (2.6), as $m = \rho V$, the curves $sin\alpha - \frac{1}{V^{\frac{1}{3}}}$ are plotted, as shown in Fig. 2.8. The curves with reaction times of 13 h and 16 h show an approximate linear tendency. For that of 18 h, it is believed that the wetting is partly in the Wenzel regime while the relationship of equation (2.6) is based on the Cassie–Baxter model. This also explains why, when the droplet volume is 0.5 μL, the sliding angle reaches 90° as the droplets stick to the surface.

2.4 Conclusions

In conclusion, Co$_3$O$_4$ superhydrophobic films were fabricated through a simple immersion chemistry approach. With increased reaction time, the microstructures can be effectively controlled from nanowire arrays to three-dimensional hierarchical

micro-flowers consisting of nanosheets as building units. Water droplets with different volumes have different contact angles and sliding angle values on the produced films, and when compared with the micro-flower structure surface, the water contact angle on the nanowire array structure surface has a higher value. The variation trend of the contact and sliding angles on the Co_3O_4 surface with an increasing reaction time is believed to generated by a reduction in surface roughness during the microstructure transformation, from high-roughness nanowire to low-roughness hierarchical micro-flower surface. Meanwhile, the experimental data of sliding angle with different droplet volumes fits well with the derived $sin\alpha - \frac{1}{V^{\frac{1}{3}}}$ relationship, except for very small droplets which is partly in the Wenzel wetting regime.

2.5 References

1. Li, J., Jing, Z., Yang, Y., Wang, Q. and Lei, Z., 2014. From Cassie state to Gecko state: a facile hydrothermal process for the fabrication of superhydrophobic surfaces with controlled sliding angles on zinc substrates. *Surface and Coatings Technology*, 258, pp.973-978.

2. Liu, M. and Jiang, L., 2010. Switchable adhesion on liquid/solid interfaces. *Advanced Functional Materials*, 20(21), pp.3753-3764.

3. Liu, X., Liu, Z., Liang, Y. and Zhou, F., 2012. In situ surface reaction induced adhesion force change for mobility control, droplet sorting and bio-detection. *Soft Matter*, 8(40), pp.10370-10377.

4. Seo, K., Kim, M. and Ahn, J.K., 2015. Effects of drop size and measuring condition on static contact angle measurement on a superhydrophobic surface with goniometric technique. *Korean Journal of Chemical Engineering*, 32(12), pp.2394-2399.

5. Wu, D., Wu, S.Z., Chen, Q.D., Zhang, Y.L., Yao, J., Yao, X., Niu, L.G., Wang, J.N., Jiang, L. and Sun, H.B., 2011. Curvature-driven reversible in situ switching between pinned and roll-down superhydrophobic states for water droplet transportation. *Advanced Materials*, 23(4), pp.545-549.

6. Wang, D., Liu, Y., Liu, X., Zhou, F., Liu, W. and Xue, Q., 2009. Towards a tunable and switchable water adhesion on a TiO 2 nanotube film with patterned wettability. *Chemical Communications*, (45), pp.7018-7020.

7. Tian, D., Chen, Q., Nie, F.Q., Xu, J., Song, Y. and Jiang, L., 2009. Patterned wettability transition by photoelectric cooperative and anisotropic wetting for liquid reprography. *Advanced Materials*, 21(37), pp.3744-3749.

8. Li, J., Liu, X., Ye, Y., Zhou, H. and Chen, J., 2011. Fabrication of superhydrophobic CuO surfaces with tunable water adhesion. *The Journal of Physical Chemistry C*, 115(11), pp.4726-4729.

9. Yin, X., Wang, D., Liu, Y., Yu, B. and Zhou, F., 2014. Controlling liquid movement on a surface with a macro-gradient structure and wetting behavior. *Journal of Materials Chemistry A*, 2(16), pp.5620-5624.

10. Li, C., Guo, R., Jiang, X., Hu, S., Li, L., Cao, X., Yang, H., Song, Y., Ma, Y. and Jiang, L., 2009. Reversible switching of water-droplet mobility on a superhydrophobic surface based on a phase transition of a side-chain liquid-crystal polymer. *Advanced Materials*, 21(42), pp.4254-4258.

11. Li, Y., Cai, W., Cao, B., Duan, G., Sun, F., Li, C. and Jia, L., 2005. Two-dimensional hierarchical porous silica film and its tunable superhydrophobicity. *Nanotechnology*, 17(1), p.238.

12. Li, Y., Huang, X.J., Heo, S.H., Li, C.C., Choi, Y.K., Cai, W.P. and Cho, S.O., 2007. Superhydrophobic bionic surfaces with hierarchical microsphere/SWCNT composite arrays. *Langmuir*, 23(4), pp.2169-2174.

13. Liu, X., Ye, Q., Yu, B., Liang, Y., Liu, W. and Zhou, F., 2010. Switching water droplet adhesion using responsive polymer brushes. *Langmuir*, 26(14), pp.12377-12382.

14. Su, Y., Ji, B., Huang, Y. and Hwang, K.C., 2010. Nature's design of hierarchical superhydrophobic surfaces of a water strider for low adhesion and low-energy dissipation. *Langmuir*, 26(24), pp.18926-18937.

15. Miwa, M., Nakajima, A., Fujishima, A., Hashimoto, K. and Watanabe, T., 2000. Effects of the surface roughness on sliding angles of water droplets on superhydrophobic surfaces. *Langmuir*, 16(13), pp.5754-5760.

16. Lopes, D.M., Ramos, S.M., de Oliveira, L.R. and Mombach, J.C., 2013. Cassie–Baxter to Wenzel state wetting transition: a 2D numerical simulation. *RSC Advances*, 3(46), pp.24530-24534.

17. Zhang, X., Guo, Y., Liu, Y., Yang, X., Pan, J. and Zhang, P., 2013. Facile fabrication of superhydrophobic surface with nanowire structures on nickel foil.

Applied Surface Science, 287, pp.299-303.

18. Lei, Y., Li, J., Wang, Y., Gu, L., Chang, Y., Yuan, H. and Xiao, D., 2014. Rapid microwave-assisted green synthesis of 3D hierarchical flower-shaped $NiCo_2O_4$ microsphere for high-performance supercapacitor. *ACS applied materials & interfaces*, 6(3), pp.1773-1780.

19. Ge, D., Wu, J., Qu, G., Deng, Y., Geng, H., Zheng, J., Pan, Y. and Gu, H., 2016. Rapid and large-scale synthesis of bare Co_3O_4 porous nanostructures from an oleate precursor as superior Li-ion anodes with long-cycle lives. *Dalton*

Transactions, 45(34), pp.13509-13513.

20.   Seo, K., Kim, M. and Ahn, J.K., 2015. Effects of drop size and measuring condition on static contact angle measurement on a superhydrophobic surface with goniometric technique. *Korean Journal of Chemical Engineering*, 32(12), pp.2394-2399.

21.   Wenzel, R.N., 1949. Surface roughness and contact angle. *The Journal of Physical Chemistry*, 53(9), pp.1466-1467.

22.   Cassie, A.B.D., 1948. Contact angles. *Discussions of the Faraday society*, 3, pp.11-16.

3.1 Introduction

Contact angle hysteresis (CAH) is one of the most important features of wetting behaviour of liquid droplets. One can easily detect the phenomena by putting a droplet on an inclined surface: the droplet becomes asymmetric and contact angle hysteresis is the difference between advancing contact angle θ_a and receding contact angle θ_r.
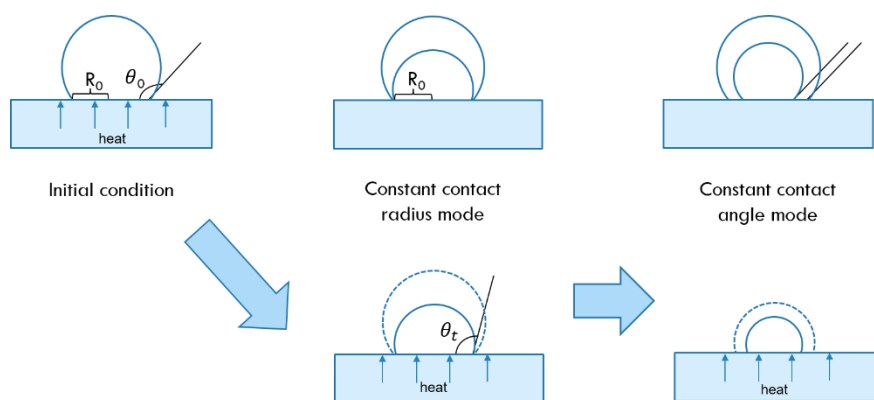
Fig. 3.1 Scheme of droplets evaporation. R_0 =contact radius, θ_0=initial contact angle, θ_r=receding contact angle.

Evaporation of sessile droplets in ambient air is a common and natural phenomenon. There has been intensive research in this area due to its significance in a variety of applications such as ink-jet printing[1], spraying of pesticides[2], spray cooling[3], lab-on-a-chip devices and DNA mapping[4]. It has been over 100 years since Maxwell first derived the relationship of this process with diffusion coefficient of the vapor, the molecular weight of the vapor, the vapor pressure, the liquid density and the temperature[5]. Later Picknett and Bexon explored and named two dominating evaporation modes, i.e. constant contact angle (CCA) mode, where the contact line

recedes with time while the contact angle remains constant, and the constant contact radius (CCR) mode where, on the contrary, the contact angle decreases as the droplet get pinned on the surface with contact radius unchanged[6]. Typically, initially evaporation begins in a CCR mode and transfers to CCA mode when the contact angle has decreased to a critical value, known as its receding angle. The proportion of each mode depends on several parameters such as substrate, liquid and temperature. In recent years, McHale et al[7], Hu and Larson et al[8], Nguyen et al[9] and Dong Hwan Shin et al[10] respectively studied the evaporation process of sessile water droplets on hydrophilic, hydrophobic and superhydrophobic surfaces. Despite the amounts of analyses devoted to this field both experimentally and theoretically, there are few if any direct studies on the effect of temperature on the process.

In this chapter, we present the experimental results of evaporating pure water droplets on different substrates, including AACVD (Aerosol assisted chemical vapour deposition) sylgard-184, TiO_2-based hydrophobic and superhydrophobic surface at a gradient of temperatures to show the effect of increasing temperature on evaporation, accompanied by a theoretical understanding.

3.2 Experimental

3.2.1 Fabrication of substrates and measurement of contact angle

The substrates were all based on glass slides and modified with coatings. Sylgard-184 silicone elastomer was purchased from Dow Corning Corporation. Fluorinated TiO_2 paint was fabricated through a simple method reported by Yao Lu[11]. By mixing two size ranges of TiO_2 nanoparticles we obtained the superhydrophobic paint and by only using one we got the less hydrophobic one.

All the coatings on glass slides can be treated as a thin film, i.e. theoretically negligible in thickness, to avoid difference in thermo-conductivity. The initial contact angles were measured with FTA-100 contact angle and droplet analyser and the data are listed below.

Surface	Static contact angle
AACVD Sylgard-184 coating	112.4 ± 9.1^0
Fluorinated TiO$_2$ coating (1)	149.8 ± 2.3^0
Fluorinated TiO$_2$ coating (2)	164.8 ± 1.0^0

Table 3.1 Initial water contact angles of different surfaces.

3.2.2 Evaporation experiments

The apparatus consists of a plate heater and a temperature sensor. All experiments were carried out at one atmosphere pressure and 30% humidity and repeated three times and averaged for accuracy. Droplets were generated with a size of 30 μL each using a pipette (Thermo Fisher Scientific Inc.). The water used in the experiments was purified with a Milli-Q system.

Evaporation was timed upon a droplet being released to the substrate, which was pre-heated to set temperature (25℃-55℃) and finished when the water droplet completely disappeared and, if applicable, the height of the stain remained unchanged for more than 10 seconds.

3.3 Theories and models

In this experiment, the water droplets sit on the surface of hydrophobic surfaces, forming a shape like a spherical cap. Here the droplet shape is decided by two parameters:

The Bond number B_o is the product of gravitational force and surface tension:

$$B_o = \frac{\rho g R h_0}{\sigma} \qquad (3.1)$$

The capillary number C_a describes the relative effect between viscosity and surface tension:

$$C_a = \frac{\mu v}{\sigma} \qquad (3.2)$$

where ρ is the density of water, g is the gravitational constant, R is the contact radius, h_0 is the initial height of droplet, σ is the air-water surface tension, μ is the dynamic water viscosity, and v is the shrinking velocity of droplet during the evaporation.

Size of the droplets in this experiment is around 30 μL, with a radius of curvature around 2.4 mm, initial height around 1.6-2.0 mm and radial evaporation velocity around 1 μm/s, the Bond number is of order 10^{-2} and the capillary number is around 10^{-8}. Hence the slight deformation in droplet shape can be ignored and the droplet can be treated like a spherical cap.

On the other hand, the evaporation rate is determined by both the vapor diffusion time and the droplet evaporation time. The characteristic diffusion time has an order of R^2/D, where D is the vapor diffusivity in air. When compared to the droplet evaporation time t, the ratio $R^2/D_t \approx c_S(1-H)/\rho$, where c_S is the saturated vapor density of water and H is the relative humidity. Here we roughly take $c_S =$

$2.31 \times 10^{-5}\,\text{g/cm}^3$ for T = 298K, H = 0.3 and $\rho = 1.0\,\text{g/cm}^3$ and the ratio = $1.62 \times 10^{-5} \ll 1$. So, the process is governed by the droplet evaporation time and can be regarded as a quasi-steady state.

To simplify, the evaporation process is considered to start in a CCR stage, until the contact angle of the droplet decreases to a threshold value θ_t. Then the mode transits from CCR to CCA until the droplet is fully evaporated.

3.3.1 Constant Contact Angle (CCA) mode

Considering a spherical droplet evaporating in an infinite medium without any boundaries, the mass of the droplet W is determined by the contact-line radius R and the contact angle θ:

$$W = \frac{\rho \pi R_s^{\,3}}{3}(1 - \cos\theta)^2\,(2 + \cos\theta) \qquad (3.3)$$

the rate of mass loss can be described as:

$$\frac{dW}{dt} = -4\pi R_s D(c_S - c_\infty) \qquad (3.4)$$

where R_s is the radius of sphere, D is the vapor diffusivity in air, c_S is the saturated vapor density of water and c_∞ the vapor density far removed from the droplet. For real droplets evaporation on a plane solid surface, Picknett and Bexon[6] mentioned that Maxwell obtained the evaporation equations using analogy between diffusive flux and electrostatic potential, and they corrected the equation by adding an $f(\theta)$ term:

$$\frac{dW}{dt} = \rho\frac{dV}{dt} = -4\pi R_s D(c_S - c_\infty)f(\theta) \qquad (3.5)$$

81

where f(θ), depending on contact angle θ, approximates the effect of the solid substrate. Apart from a complex integration, they expressed the resulting values of $f(\theta)$ using a polynomial fit:

$$2f(\theta) = \begin{cases} 0.6366\theta + 0.09591\theta^2 - 0.06144\theta^3 & (0 \le \theta < 10°) \\ 0.00008957 + 0.6333\theta + 0.116\theta^2 - 0.08878\theta^3 \\ \quad +0.01033\theta^4 \\ (10° \le \theta \le 180°) \end{cases} \qquad (3.6)$$

For the constant contact angle mode, $\theta = \theta_t$, $f(\theta) = f(\theta_t)$, and H = 0.3, thus (3.5) can be integrated by incorporating (3.3):

$$\text{droplet lifetime} = t_{CCA-PB} = \frac{\rho R_{S0}{}^2 (1-\cos\theta_t)^2 (2+\cos\theta_t)}{4D(c_S - c_\infty)f(\theta_t)} \qquad (3.7)$$

where according to an empirical fit[12],

$$c_s - c_\infty = c_s(1-H) \approx 0.7 * (6.335 + 0.6718T_c - 0.020887T_c^2 + 0.00073095T_c^3)$$

$$T_c = \text{Celsius temp} \qquad (3.8)$$

And from Chapman–Enskog theory[13] we have the diffusion coefficient under different temperature:

$$D = \frac{1.858 \times 10^{-3} T^{3/2} \sqrt{1/M_1 + 1/M_2}}{p\sigma_{12}^2 \Omega} \qquad (3.9)$$

where Ω is temperature-dependent, thus

$$\frac{D_1}{D_2} = \left(\frac{T_1}{T_2}\right)^{\frac{3}{2}} \left(\frac{\Omega_2}{\Omega_1}\right) \qquad (3.10)$$

For water vapour in air, as $D_{T=298K} = 0.264 \, cm^2/s$, using a linear interpolation for Ω we obtain:

$$D \approx 0.264 \left(\frac{T}{298}\right)^{\frac{3}{2}} \left(\frac{1.334}{1.936 - 0.00202T}\right) \qquad (3.11)$$

82

In addition to this, Erbil and his co-workers have come up with an equation that can be used as an indication of constant contact angle mode[14].

For a spherical-cap-like droplet, its volume

$$V = \frac{\pi R^3 (1-\cos\theta)^2 (2+\cos\theta)}{3\sin^3\theta} \qquad (3.12)$$

In the CCA stage, the contact angle of droplet remains unchanged while the contact area diminishes. The variation rate of its volume can be worked out by taking partial derivative with time:

$$\frac{dV}{dt} = \frac{\pi R^2 (1-\cos\theta)^2 (2+\cos\theta)}{\sin^3\theta} \left(\frac{dR}{dt}\right) \qquad (3.13)$$

Following Fick's Law, Rowan et al[15] assumed that evaporation rate is given by

$$\frac{dV}{dt} = -\frac{D}{\rho} \int \nabla c \cdot d\vec{S} \qquad (3.14)$$
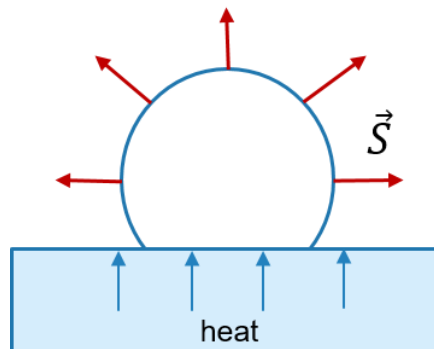
Fig. 3.2 The assumed uniform outer diffusion flux from droplet surface.

for cases driven by gradient of vapor concentration, where $\vec{s}$ is the vector of outer direction of spherical cap surface. As mentioned above, the process can be regarded as quasi-steady so here the diffusion flux is assumed to be uniformly radially

outward. Thus, the right-hand side of (3.14) can be integrated using the surface area of spherical cap:

$$\frac{dV}{dt} = -\frac{D}{\rho}(c_S - c_\infty) \cdot S = -\frac{2\pi DR^2}{\rho(1+\cos\theta)}(c_S - c_\infty) \qquad (3.15)$$

Incorporating (3.15) into (3.13) gives

$$\frac{R(1-\cos\theta)(2+\cos\theta)}{3\sin^2\theta}\left(\frac{dR}{dt}\right) = -\frac{2D}{\rho}(c_S - c_\infty) \qquad (3.16)$$

Solving (3.16) we obtain

$$R_0^2 - R^2 = \frac{4D(c_S-c_\infty)\sin^2\theta_t}{\rho(1-\cos\theta_t)(2+\cos\theta_t)}t \qquad (3.17)$$

where R_o is the initial contact radius and R is the radius at time t. By setting R = 0 gives the droplet lifetime

$$t_{CCA-E} = \frac{(1-\cos\theta_t)(2+\cos\theta_t)\rho R_0^2}{4D(c_S-c_\infty)\sin^2\theta_t} \qquad (3.18)$$

3.3.2 Constant Contact Radius (CCR) mode

Picknett and Bexon mentioned in their work that for constant contact radius mode, there was no expression similar to (3.7) while it was derivable by numerical integration[6]. McHale et al adopted (3.6) and gained an analytical function of the contact angle[7].

In (3.12), given that R is constant, the rate of change of droplet volume can be written as

$$\frac{dV}{dt} = \frac{-\pi R^3}{(1-u^2)^{1/2}(1+u)^2}\left(\frac{du}{dt}\right) \qquad (3.19)$$

where u = cosθ. Combining (3.13) and (3.5) we obtain

$$\frac{1}{2f(\theta)(1+u)^2}\left(\frac{du}{dt}\right) = \frac{2D(c_S-c_\infty)}{\rho R^2} \qquad (3.20)$$

Then McHale et al used a polynomial fit to $^1/_{2f(\theta)}$:[7]

$$\frac{1}{2f(\theta)} \approx \sum_{n=0}^{3} d_n u_n = 0.999766 + 0.481517u + 0.292040u^2 + 0.089118u^3 \qquad (3.21)$$

based on the theory of Picknett and Bexon (3.6) in range $90° - 180°$. Now incorporating (3.21) into (3.20) we have

$$F(\theta) \equiv \frac{-0.721171}{1+\cos\theta} + 0.164791\ln(1+\cos\theta) + 0.113804\cos\theta + 0.044559\cos^2\theta$$

$$= \frac{-2D(c_S-c_\infty)t}{\rho R^2} + F(\theta_0) \qquad (3.22)$$

where $F(\theta_0)$ is the value of the left-hand side of (3.16) at the initial contact angle. Set $\theta = \theta_t$, as the contact angle will reach θ_t at the end of CCR stage, we obtain

$$t_{CCR-M} = \frac{[F(\theta_t)-F(\theta_0)]\rho R_0^2}{-2D(c_S-c_\infty)} \qquad (3.23)$$

3.3.3 Evaporative cooling effect

During the process, the latent heat of evaporation will result in the cooling down at the droplet surface and therefore reduce the evaporation flux. This effect is negligible at low temperature but it can become considerable as the temperature rises.

Y Wang et al[16] have adopted finite element method to study the effects of substrates properties on the evaporation of sessile droplets, including thermo-conductivity, thickness and temperature. In the paper they applied a dimensionless parameter-evaporative cooling number E_c, to characterize the reduction of evaporative flux caused by evaporative cooling.

$$E_c = \frac{H_L Db}{k_w} \qquad (3.24)$$

In the equation, H_L is the latent heat of evaporation, $b = \frac{dc_s}{dT}|_{T=T_{room}}$ and k_w is the heat conductivity of water. As they claimed, $E_c=1$ is known as the critical value. When $E_c<1$, the evaporation rate changes very slightly as E_c changes (10% reduction as maximum).

In calculation, the approximation of temperature-dependent H_L and k_w is approached using linear interpolation within the temperature range.
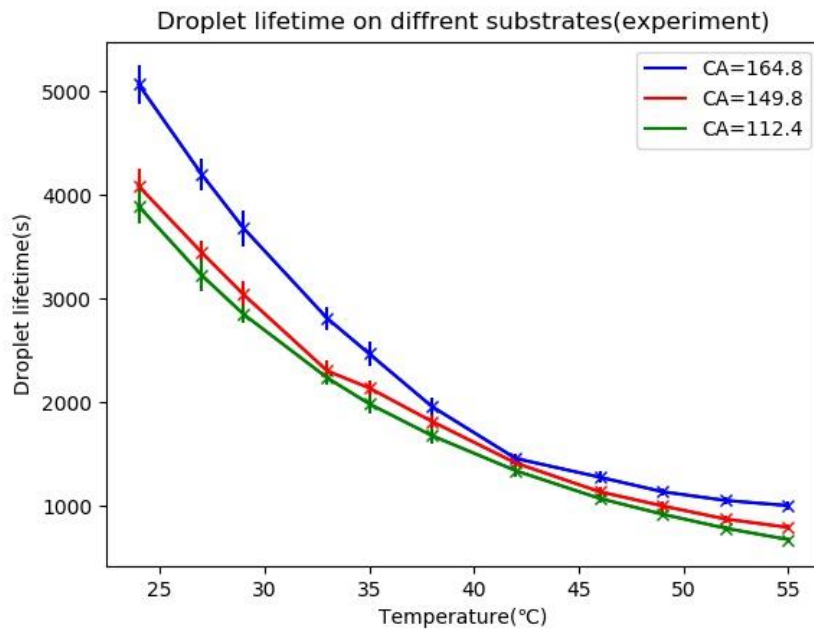
Fig. 3.3 Evaporation lifetime of water droplets on three different substrates, experiment data.

3.4 Results and discussion

3.4.1 Evaporation lifetime-experimental result

Shown in Fig. 3.3 are the lifetime of water droplets on surfaces with different initial contact angles. Two main theories have been reported by previous researchers to

explain the influence of contact angle. W Xu et al[17] considered that the solid substrate restricts the vapor diffusion in the wedge-shape space between substrate and droplets when contact angle increases, while Susmita Dash[18] has attributed it to evaporative cooling effect at the droplet interface.

To compare two approaches to model data on evaporation with CCA mode, the lifetime curves were studied by putting experimental and CCA-modelling data (let $\theta_t = \theta_0$, i.e. assume that the whole process takes place in CCA stage) in one graph, as in Figure 3.4.

When CA = 164.8°, as the surface has a very high water contact angle and low hysteresis, most of the evaporation process should happen in a CCA mode. Therefore, t_{CCA-E} is adopted as the more accurate model in the CCA stage.

3.4.2 Transition between two modes

Now consider the droplet with initial parameters $\theta = \theta_0, R = R_0$ which starts to evaporate in CCR stage. After $t_{CCR-M} = \frac{[F(\theta_t)-F(\theta_0)]\rho R_0{}^2}{-2D(c_S-c_\infty)}$, as θ drops to θ_t, the CCA mode follows with $\theta = \theta_t$, $R = R_0$, which takes $t_{CCA-E} = \frac{(1-cos\theta_t)(2+cos\theta_t)\rho R_0^2}{4D(c_S-c_\infty)sin^2\theta_t}$ to finish.

Thus, the total droplet lifetime:

$$t_{total} = t_{CCR-M} + t_{CCA-E} = \frac{[F(\theta_t)-F(\theta_0)]\rho R_0{}^2}{-2D(c_S-c_\infty)} + \frac{(1-cos\theta_t)(2+cos\theta_t)\rho R_0^2}{4D(c_S-c_\infty)sin^2\theta_t} \qquad (3.25)$$

By assigning the experimental data points (t and T) to (3.25), the value of θ_t is decided.

However, as it's still hard to work out θ_t from the right-hand side of (3.25), the function curves of $t_{total}(\theta)$ are drawn in the range of $\theta \in (90°, \theta_0)$, since $\theta \in (90°, 180°)$ for the valid range of t_{CCR-M}, as shown in Fig. 3.5 below.

Then the values of θ_t can be obtained by locating the corresponding t_{total} values in these curves. An example has been illustrated in the figure. The results are shown below in Fig.3.6.

3.4.3 Evaporative cooling

To investigate the influence of evaporative cooling on evaporation rate, E_c is calculated and plotted as a function of temperature in Fig. 3.7. From the figure it can be seen that E_c increases monotonically as temperature rises and $E_c<1$ when 25℃ < T < 55℃. Thus, only minor change in evaporation time will be observed.
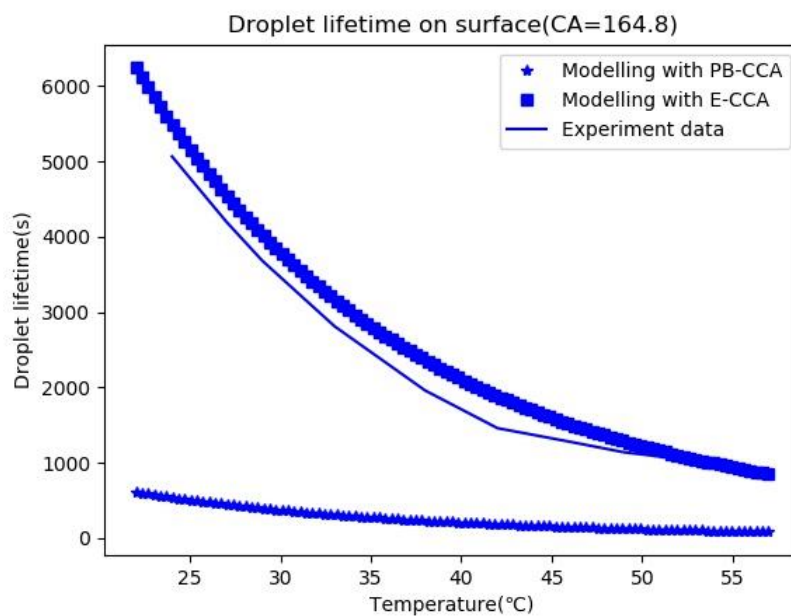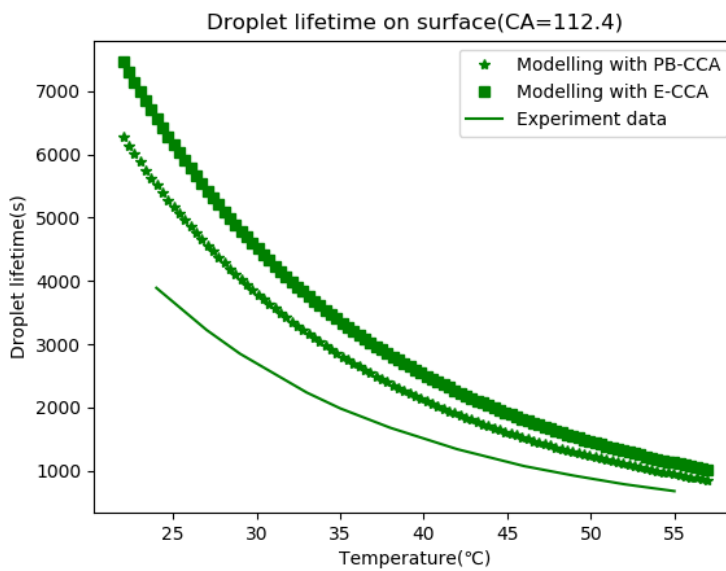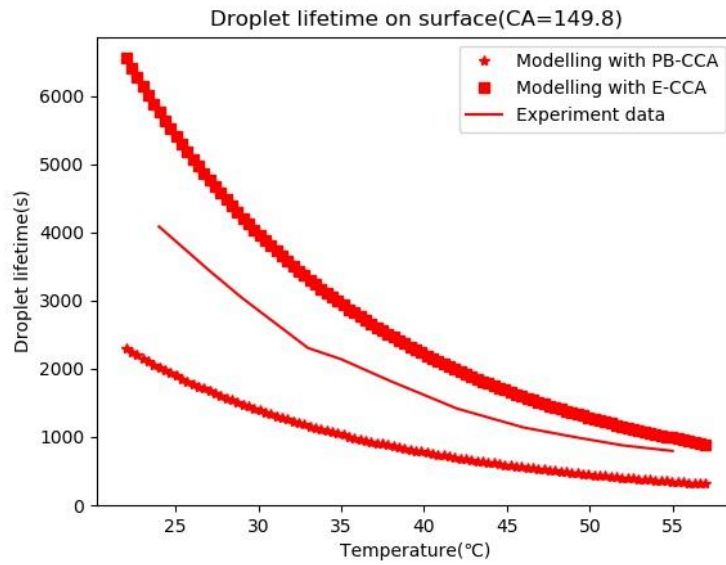
Droplet lifetime on surface(CA=149.8)

Droplet lifetime on surface(CA=112.4)

Fig. 3.4 Experimental and CCA-modelling droplets lifetime on three substrates. When CA = 164.8°, all three curves descend with temperature and the experimental curve almost follows the stages of the Erbil-CCA one.

Ttotal-Theta on surface(CA=164.8)

Ttotal-Theta on surface(CA=149.8)

(143.1, 3041)

Ttotal-Theta on surface(CA=112.4)

90
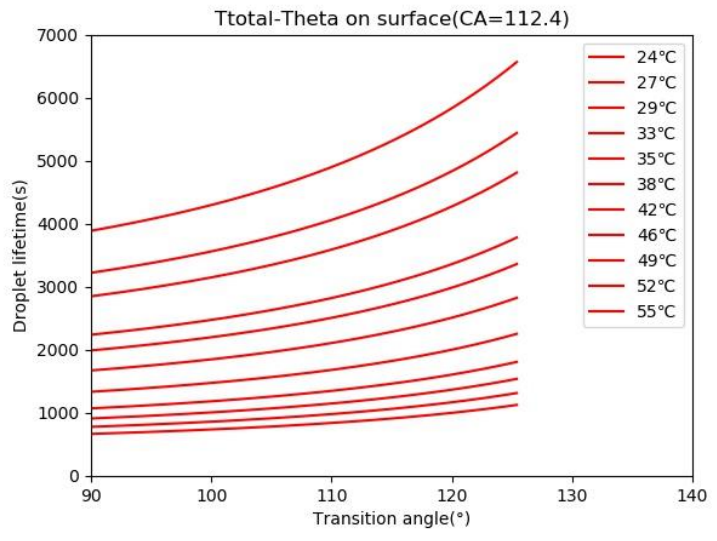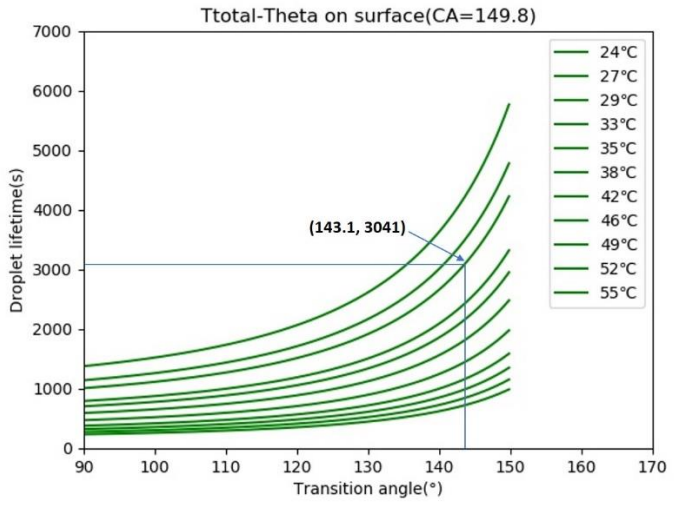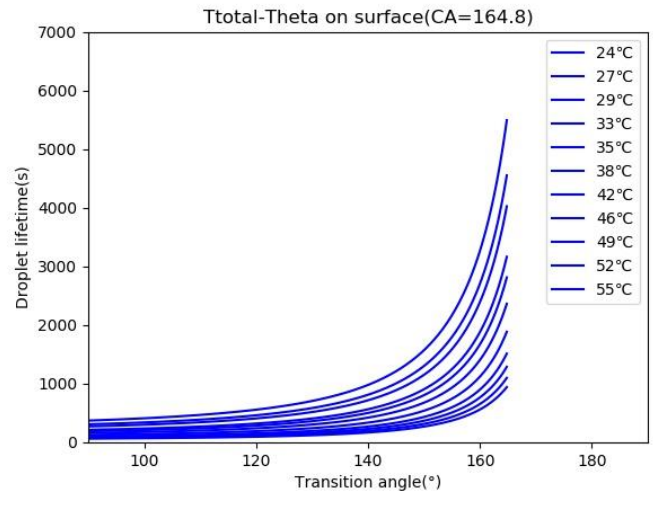
Fig. 3.5 The curves of $t_{total} - \theta$ are plotted as experimental data points to find out the value of θ_t.
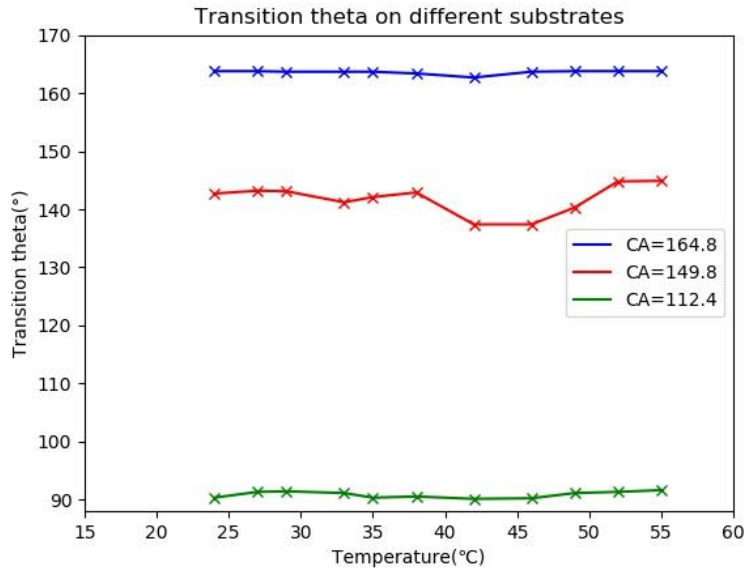
Fig. 3.6 θ_t where CCR stage transits to CCA state on different substrates.
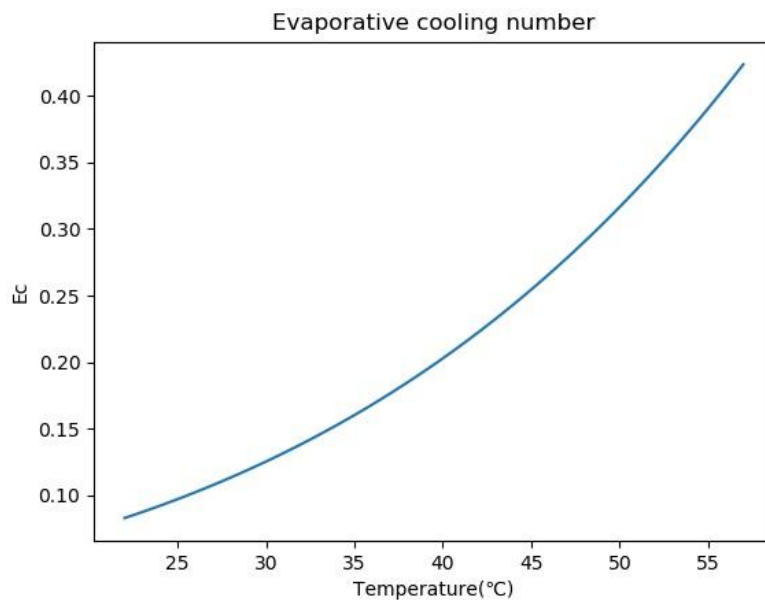
Fig. 3.7 The evaporative cooling number E_c vs temperature.

3.4.4 Analysis

The values of transition angles given by calculation (θ_t) are close to the receding angles (θ_R) from droplet measurement, showing a good fitting between the models and the experiment. The existing error can be explained by two main factors: 1. The accuracy of adopted models and 2. The simplification of evaporation process. Commonly droplet evaporations will not be purely CCR or CCA. A mixed stage and the wetting mode transition will probably occur. Moreover, even in a CCR or CCA period, the contact radius/contact angle will still undergo minor changes.

From Fig. 3.6 we can see that $\theta_t \approx 163°$ for surface whose CA = 164.8°, which means its evaporation process is almost in CCA mode. Taking no account of discrepancy, this can be achieved and has been reported on some superhydrophobic surfaces with both extremely high contact angle and low hysteresis.

The θ_R for surface CA = 149.8°/112.4° are approximately 143°/91°, respectively. The transition angle varies slightly with temperature, showing a descending trend at $30℃ < T < 40℃$ and a rising after $T > 45℃$. This is consistent with the variation tendency of droplet lifetime in Fig.3.4, that the average evaporation rate slows down after $T > 45℃$, given the fact that a droplet evaporating with a CCR mode will have a shorter lifetime than a droplet experiencing CCA mode of evaporation, due to the liquid-air contact area.

The fact that evaporation rate slows down, with a relatively shorter CCR stage and longer CCA stage at higher temperature is consistent with the calculation of an evaporative cooling effect. According to Fig. 3.7, if the temperature continues rising, reduction in evaporation rate caused by evaporative cooling at the surface will be more obvious as E_c increases and exceeds 1.

This result may be of help in the deposition of nanofluids where the CCR stage should usually be avoided as nanoparticles would accumulate at the edge of contact line, leading to a deposition ring but waste inside.

3.5 Conclusions

The evaporation process of water droplets was studied experimentally with a gradient of temperatures and different substrates. Several theoretical models have been adopted to simulate the CCR-CCA evaporation process. As some simplification and approximation methods were employed, such as neglecting the third 'mixed' mode and accepting the accuracy of the models, discrepancy would exist. However, the modelling results fit well with experimental data.

A phenomenon has been noticed that the evaporation rate reduces at relatively higher temperature ($T > 45℃$), which is attributed to the influence of a self-cooling effect. This result can be made use of for a denser deposition, which is fabricated by droplet evaporation on a superhydrophobic surface at high temperature.

3.6 References

1.   Kim, D., Jeong, Y., Song, K., Park, S.K., Cao, G. and Moon, J., 2009. Inkjet-printed zinc tin oxide thin-film transistor. *Langmuir*, *25*(18), pp.11149-11154.

2.   Yu, Y., Zhu, H., Frantz, J.M., Reding, M.E., Chan, K.C. and Ozkan, H.E., 2009. Evaporation and coverage area of pesticide droplets on hairy and waxy leaves. *Biosystems Engineering*, *104*(3), pp.324-334.

3.   Jia, W., Aguilar, G., Wang, G.X. and Nelson, J.S., 2004. Heat-transfer dynamics during cryogen spray cooling of substrate at different initial temperatures. *Physics in Medicine & Biology*, *49*(23), p.5295.

4.   Wu, A., Yu, L., Li, Z., Yang, H. and Wang, E., 2004. Atomic force microscope investigation of large-circle DNA molecules. *Analytical biochemistry*, *325*(2), pp.293-300.

5.   Weon, B.M., Je, J.H. and Poulard, C., 2011. Convection-enhanced water evaporation. *Aip Advances*, *1*(1), p.012102.

6.   Picknett, R.G. and Bexon, R., 1977. The evaporation of sessile or pendant drops in still air. *Journal of Colloid and Interface Science*, *61*(2), pp.336-350.

7.   McHale, G., Aqil, S., Shirtcliffe, N.J., Newton, M.I. and Erbil, H.Y., 2005. Analysis of droplet evaporation on a superhydrophobic surface. *Langmuir*, *21*(24), pp.11053-11060.

8.   Hu, H. and Larson, R.G., 2002. Evaporation of a sessile droplet on a substrate. *The Journal of Physical Chemistry B*, *106*(6), pp.1334-1344.

9.   Nguyen, T.A. and Nguyen, A.V., 2012. Increased evaporation kinetics of sessile droplets by using nanoparticles. *Langmuir*, *28*(49), pp.16725-16728.

10.   Shin, D.H., Lee, S.H., Jung, J.Y. and Yoo, J.Y., 2009. Evaporating characteristics of sessile droplet on hydrophobic and hydrophilic surfaces. *Microelectronic Engineering*, *86*(4-6), pp.1350-1353.

11. Lu, Y., Sathasivam, S., Song, J., Crick, C.R., Carmalt, C.J. and Parkin, I.P., 2015. Robust self-cleaning surfaces that function when exposed to either air or oil. *Science, 347*(6226), pp.1132-1135.

12. R Nave. Empirical fit of saturated vapor density versus Celsius Temperature. [online]. Georgia State University. Available from: http://hyperphysics.phy-astr.gsu.edu/hbase/Kinetic/relhum.html [Accessed 8 August 2019].

13. Slattery, J.C. and Bird, R.B., 1958. Calculation of the diffusion coefficient of dilute gases and of the self-diffusion coefficient of dense gases. AIChE Journal, 4(2), pp.137-142.

14. Erbil, H.Y., 2012. Evaporation of pure liquid sessile and spherical suspended drops: A review. *Advances in colloid and interface science, 170*(1-2), pp.67-86.

15. Rowan, S.M., Newton, M.I. and McHale, G., 1995. Evaporation of microdroplets and the wetting of solid surfaces. *The Journal of Physical Chemistry, 99*(35), pp.13268-13271.

16. Wang, Y., Ma, L., Xu, X. and Luo, J., 2015. Combined effects of underlying substrate and evaporative cooling on the evaporation of sessile liquid droplets. *Soft matter, 11*(28), pp.5632-5640.

17. Xu, W., Leeladhar, R., Kang, Y.T. and Choi, C.H., 2013. Evaporation kinetics of sessile water droplets on micropillared superhydrophobic surfaces. *Langmuir, 29*(20), pp.6032-6041.

18. Dash, S. and Garimella, S.V., 2013. Droplet evaporation dynamics on a superhydrophobic surface with negligible hysteresis. *Langmuir, 29*(34), pp.10785-10795.

4.1 Introduction

Droplet collision is common in nature[1] such as in rain, waterfalls and rivers. The importance of droplet collisions was first recognized in the context[2] of rainfall as a liquid phase dispersed in ambient air. Droplet collision also happens in common industry processes, such as in the ignition or combustion process[3] and in surface spray processes[4]. The collision between droplets has attracted scientists' attention since 1879 when Lord Rayleigh found that small rain droplets bounced after colliding with a larger pool of water. He attributed the failure of coalescence to the trapped air layer between the interface of the droplet that prevented the contact of droplets. In the following decades, investigations have[5] focused on binary droplets collision at different sizes to understand the process of rainfall. In the 1990s, the attention in this area was paid to the collision state of water and hydrocarbon droplets[6-10] for the research of fuel spray process in combustion. Among these studies, Jiang[10] and co-workers drew a map of binary droplet collision states using Weber Numbers and impact parameters.

Despite the efforts in this field, most of them ignored the temperature effect on the outcomes of the collision process. To the best of our knowledge, all the previous studies were conducted assuming binary droplets that share the same temperature, which is rather unlikely in a real industrial process, and it is already reported that temperature has a strong impact on the ratio of coalescence and rebound during the binary droplet collision[11]. This work was focused on binary-droplet collisions and coalescence and the rebound behaviour of the binary droplets was studied. To clearly observe the change of interface during the coalescence process, a dye was used in the stationery phase.

4.2 Experimental

4.2.1 Fabrication of a Si-based superhydrophobic surface

The chemicals used in the fabrication of Si superhydrophobic surfaces are as follows: silver nitrate (99.8%); acetone (99.5%); ethanol (99.7%); hydrogen peroxide (30%); hydrofluoric acid (40%); ferric nitrate (98.5%); Perfluoro-1,1,2,2-tetrahydrooctyltrichlorosilane (97%).

The superhydrophobic silicon plate was generated via silver assisted etching[12] followed by salinization with fluorosilane[13]. The static water contact angle of the plate was about 155.6⁰.

4.2.2 Pump and imaging system setup

Fig 4.1 demonstrates the experimental setup. The stationary droplet on the superhydrophobic substrate was aligned to the impacting droplet by the micro-positioning stage. A syringe pump and a needle with inner-diameter 0.3 mm were used to generate droplets with diameter of 2 mm. A heating system (DIYCH401, Shanghai Hua Jian Electric Heating Appliance Co. Ltd, China) was used to adjust the temperature of the syringe between room temperature and 100℃.

Imaging hardware used in the setup included a high-speed camera (X-Stream XS-4, IDT, US), a magnification zoom lens (XDS-0745, JANUS, China) with 3* magnification, and an LED light source (C-F1230, Nikon, Japan). Another high-speed camera (AOS, CH) was set at side to ensure a head-on collision.

The impact parameter and impact velocity were obtained through analysis of the high-speed video images using the motion studio software. The superhydrophobic

substrate with stationary droplet on top was placed on the 3D micro‑positioning

stage, and the stage was adjusted to obtain a release height of 13 mm, between the

tip of the needle and the substrate. The experiments were conducted at room

humidity (50%) to minimize the impact of humidity.
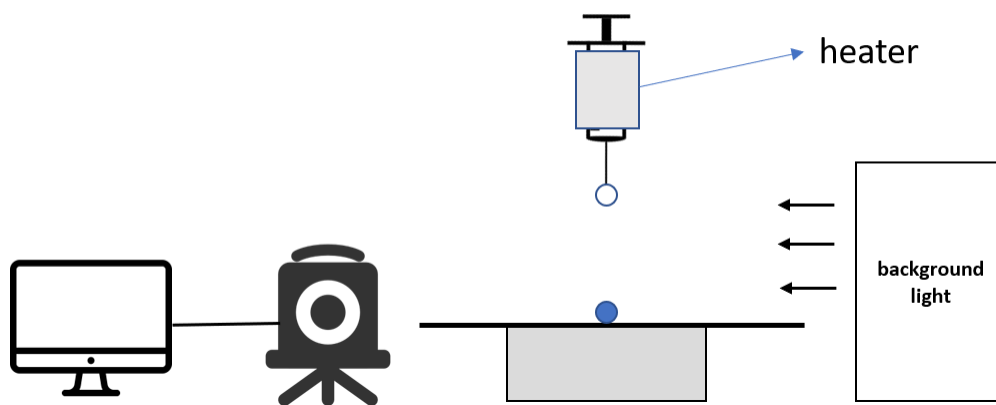
Fig. 4.1 The photo and scheme of the substrate, syringe pump and imaging system.

4.3 Results and discussion

4.3.1 Temperature-dependent deformation before coalescence

The coalescence process was studied and compared first when impacting droplets were set with temperature 27℃ and 40℃. At 27℃, the head-on collision process proceeded with a large deformation of both droplets. At the beginning, the impacting droplet fell and contacted with the stationary one on the superhydrophobic surface. Due to the air layer trapped at the interface, the two droplets didn't merge but deformed like elastic balls. It is believed that the kinetic energy converted to the surface energy here, and they would not merge together until they reached the maximum spreading area.
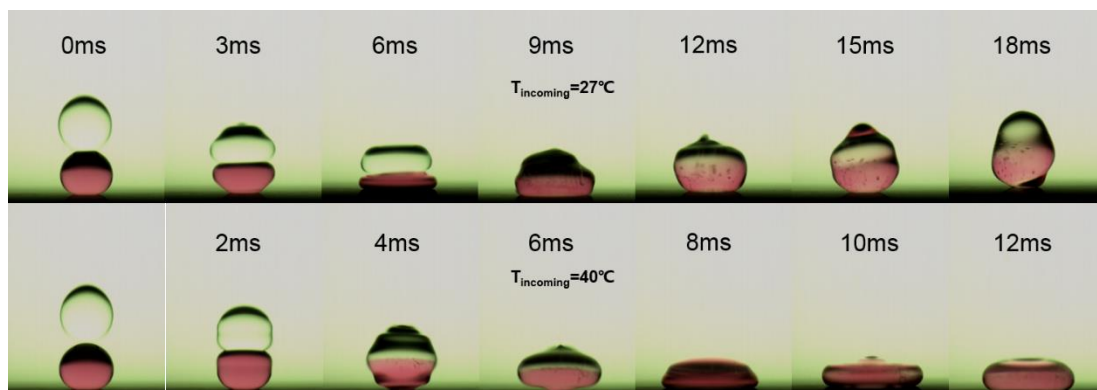
Fig. 4.2 The process of droplets collision at temperature of 27℃ and 40℃

As shown in Figure 4.2, the coalesce process time is different when the temperature of the released drop was raised to 40℃. Firstly, it took a shorter time for the two droplets to merge just 2 ms ~ 4 ms after contacting. No large deformation was observed before the coalescence. Then, as the process moved forward, a clear and

flat interface appeared in the middle of the merged droplet. Afterwards the merged droplet recoiled and rebounded as if a single droplet colliding on a solid surface.

Two possible factors were considered as possible explanations for the differences: surface tension and surrounding vapour.

As the temperature rises, surface tension will decrease while the surrounding vapour pressure, on the contrary, increases. A lower surface tension can make merger of the droplets much easier[9], but the change of surface tension is quite small from 25 ℃ to 40 ℃. (from 71.99 to 69.60 mN/m)[14].

The second factor is the surrounding vapour, whose influence can be ignored at room temperature. But as the temperature rises, the vapour pressure and condensation will significantly increase, which is beneficial to coalescence because of, expectedly easier formation of a liquid bridge by vapour condensation at the interface between two droplets[15]. It is out of the same reason that the humidity of air needs to be controlled. Figure 4.3 shows the images of the merging moment at different temperatures. A clear difference can be observed between those below 40℃ and those above 40℃ - at lower temperatures droplets look elastic and robust. They collided and squashed are before finally merging at the interface, while at higher temperatures the merging process seemed to begin at the first millisecond after the two droplets have been in contact. The air film trapped at the interface was easily broken.
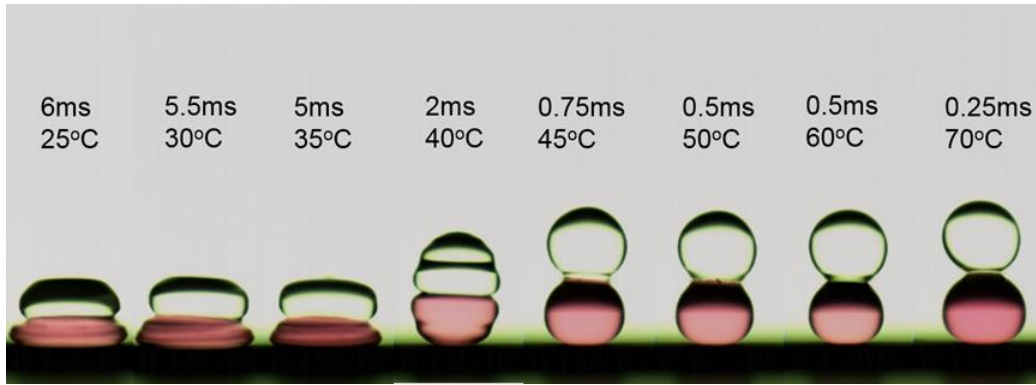
Fig. 4.3 The merging moment of droplets colliding at different temperatures of impacting droplets.

4.3.2 Surface contact time

The contact time is defined as the time when a merged droplet is in contact with the superhydrophobic surface before rebounding from it. It is often a crucial parameter for the interaction between droplet and surface. As it is shown in figure 4.4, the curve shows that all collision processes at various temperatures remain constant at about 25 ms. This trend can be explained by balancing inertia (of the order $\rho R/\tau^2$, ρ: fluid density, R: droplet radius, τ: contact time) with capillarity[16] (γ/R^2, γ: surface tension), which yields $\tau \sim \sqrt{\frac{\rho R^3}{\gamma}}$. It could be obtained that when ρR is almost fixed, the contact time τ is only related to surface tension γ, which again indicates the surface tension is not a crucial factor for coalescence.
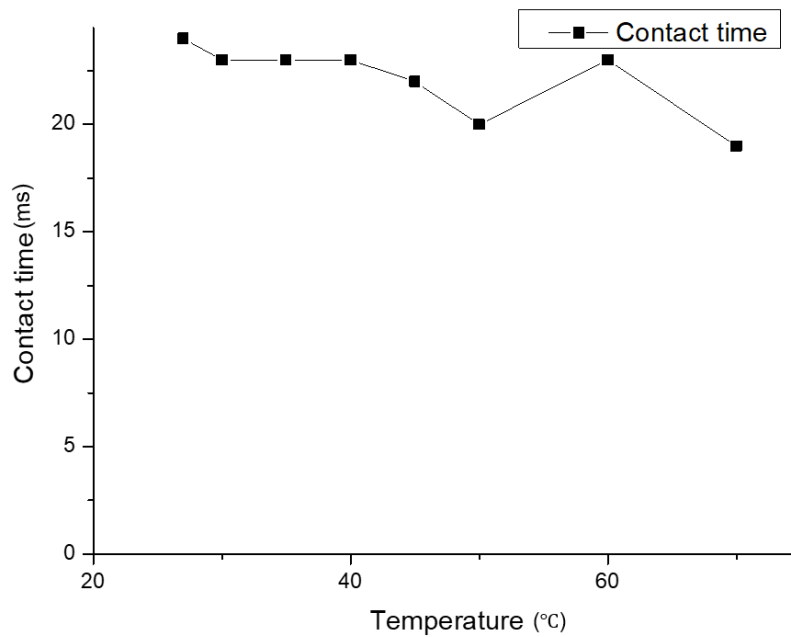
Fig. 4.4 The contact time of droplets collision at different temperatures

4.3.3 Energy conversion

Energy conversion should always be taken into consideration to study the intrinsic mechanism. Figure 4.5 serves to evaluate the spreading and rebounding behaviour of droplet collision at various temperatures. The plots show the relationship between the dimensionless spread length $\Psi = \frac{spread\ length}{initial\ radius}$ and time t in milliseconds, which describe the movement of the merged droplet on the surface.

Several interesting trends can be found in Figure 4.5. At a temperature of 27℃, the max spread length, which can be regarded as a parameter of the remaining energy after coalescence, was about 1.3. However, when the temperature increased to 45℃, the max spread length increased to 1.6 and then stayed around that even at higher temperatures.
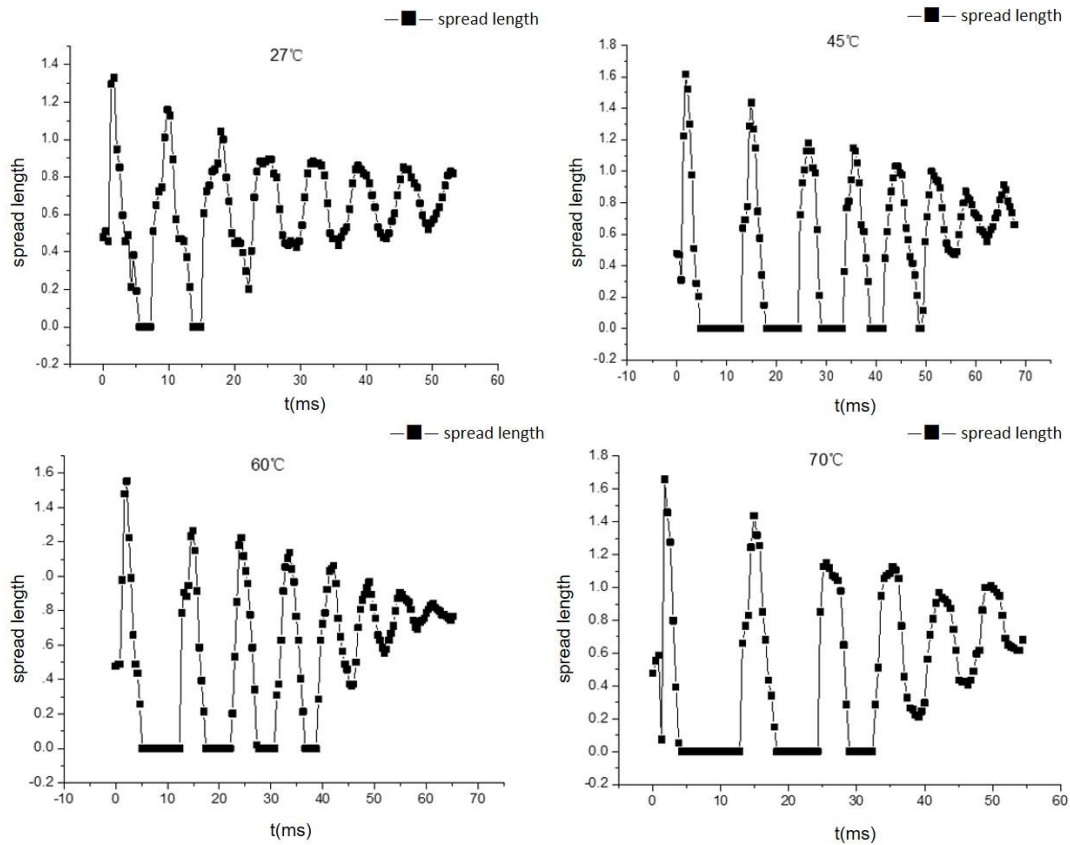
Fig. 4.5 The relationship between spread length and time during an impact at different temperatures.

Another interesting statistic is the numbers of droplet bounces at different temperatures. As shown in the figure, the merged droplet only rebounded twice at 27℃. However, it bounced 5 times at 45℃. With the further increase of the temperature, the number of bounces decreased to 4 times and 3 times at 60 and 70℃. It is believed that the difference in both spreading length and the number of bounces after coalescence can be attributed to energy dissipation during the coalescence.

Here the energy of two droplets at the initial stage can be roughly considered as the sum of surface energy of two droplets and the gravitational potential energy of the

impacting droplet. During the falling process of the impacting droplet, the gravitational potential energy is converted to kinetic energy. Droplets began to deform after colliding, and the kinetic energy is transformed to the surface energy.

When the surface energy reached its maximum value at the max spread length, the kinetic energy was zero at that moment. Energy dissipation occurred in this process and can be probably related to three factors: the viscosity loss, the velocity distribution in merged droplet and the wetting property of the surface.

Viscosity dissipation is common during the droplet movement. For water, the dynamic viscosity η is less than 10^{-3} Pa.s at room temperature[17]. Reynolds number ($Re = \rho u R / \eta$, u: relative velocity of the fluid) can be adopted as a simple indication of the ratio between the energy dissipated in viscosity and stored as the surface energy. In this case, the Reynolds number was more than 500, which indicates that the viscosity dissipation could be ignored[18]. From another point of view, the contact time was only about 20 ms which is too short to cause a large viscosity dissipation. Although the viscosity of water sharply increases as the temperature rises, the influence will remain negligible.

Apart from viscosity, velocity distribution also needs to be considered in the process. Part of the horizontal velocity is possibly transferred into internal vibration during the spread and recoil process, especially at low temperature. Also, as droplets deformed tremendously before merging at lower temperature, inner mixing and rotation will occur after merging happens, which will induce a huge loss of kinetic energy. The movement of red dye in the stationary droplet shows these phenomena clearly.

The wetting property of a surface also played an important role in the energy loss during coalesce and rebounding process of the colliding binary droplets. Imagine that

a relatively hot droplet was released and collided with a room-temperature one. Heat transfer started to take place as the two droplets collided, and was accelerated after the merging process, which balanced the temperature at different parts of the merged droplet and, consequently, increased the temperature at the solid-water interface. For droplets on superhydrophobic surfaces, contact angle will reduce as the temperature of droplets rises, as higher temperature results in a more violent molecular movement which diminish the intermolecular force and hence the surface tension. Simultaneously, vapour pressure will also be strengthened at the interface. The vapour could condense on the relatively cold superhydrophobic surface. The combination of these factors made the droplet stuck on the surface. This explains why the maximum spread length remains 1.6 at high temperature while the number of bounces decreases.

The Restitution Coefficient is a key parameter used to evaluate the kinetic energy loss during the coalescence process. It is defined as the ratio of impacting velocity and rebound velocity[19]. Figure 4.6 shows a large jump in the coefficient between 35℃ and 40℃, which sets the boundary between the two types of coalescence process. At lower temperatures, the value of the Restitution coefficient is about 0.25~0.3. Huge energy loss could be inferred from the chaotic mixing process recorded by the images. However, when the temperature of impacting droplet reaches 40℃, the coefficient approaches 0.5 and the energy loss is relatively small.
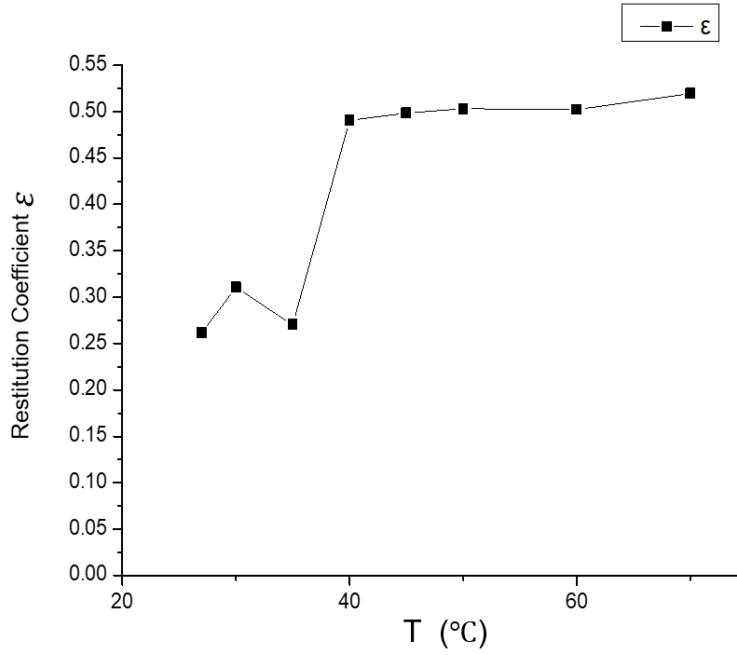
Fig. 4.6 The Restitution Coefficient at different temperatures in this experiment.

Finally, the surface energy and kinetic energy during the coalescence process were estimated with simplifications: at the very beginning, the total energy is the sum of surface free energy of both droplets and the gravitational potential energy of the impacting one. When the merged droplet spread on the solid surface and reached a max area, all energy was converted to surface energy (droplet height neglected). Then kinetic and surface energy were converted into each other during the impacting-spreading-recoil cycles. Then we can get:

$$KE_1 = mg\Delta h \qquad (4.1)$$

When in the air, the surface free energy of impacting droplet can be roughly evaluated as:

$$G_1 = 4\pi R^2 \gamma \qquad (4.2)$$

The surface free energy of the stationery droplet[20]:

$$\frac{G_2}{\sqrt[3]{9\pi}V^{2/3}\gamma} = (1 - cos\theta)^{2/3}(2 + cos\theta)^{1/3} \qquad (4.3)$$

where V, θ are the liquid volume and contact angle.

As the binary droplets collided and merged, the mixed droplet reached the max spread area on the surface and all converted into surface energy:

$$G_{mix} = \pi R_{max}^2 \gamma (1 - cos\theta_a) \qquad (4.4)$$

where θ_a is the advancing contact angle.

Figure 4.7 illustrates the estimated surface and kinetic energy fluctuations at temperature 27 and 45℃.

At 27℃, the dissipation on collision was so large that almost all the kinetic energy was lost, the surface energy received only a very small portion and slightly increased. The merged droplet could hardly rebound, and the energy transition was almost complete. Contrary to the condition at 27℃, the energy loss during the initial collision at 45℃ was much smaller. The energy conversion persisted as the droplet recoiled for several times, shown as fluctuations in the graph.
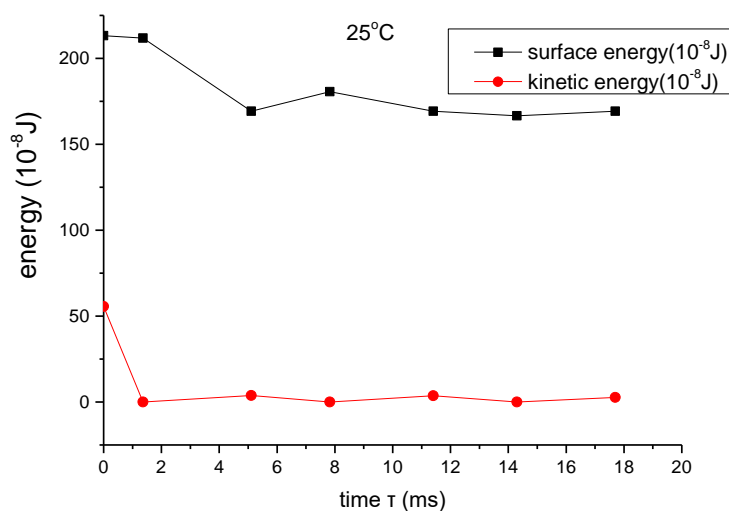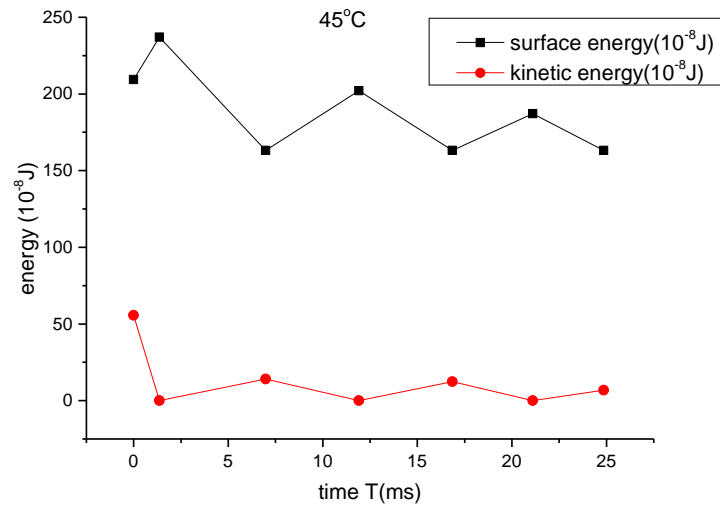
Fig. 4.7 The simulation of changes in droplets surface and kinetic energy at 27℃ and 45℃, indicating two different collision types.

4.4 Conclusions

In this chapter, the dynamic process of the droplets' collision on superhydrophobic surface has been discussed, the temperature-induced co-coalescence process was also studied in detail. Changes in temperature will lead to two different dynamic behaviours of the coalescence process: At low temperature (room temperature), the droplets collisions normally go through a long merging time with huge energy loss, while the process tends to be much faster and energy-saving at high temperature. The finding can help further evaluate the collision process and may possibly offer a solution to droplets adhesion in industrial field.

4.5 References

1.   Brazier-Smith, P.R., Jennings, S.G. and Latham, J., 1971. Accelerated rates of rainfall. *Nature*, 232(5306), p.112.

2.   List, R. and Gillespie, J.R., 1976. Evolution of raindrop spectra with collision-induced breakup. *Journal of the Atmospheric Sciences*, 33(10), pp.2007-2013.

3.   Nikolopoulos, N., Nikas, K.S. and Bergeles, G., 2009. A numerical investigation of central binary collision of droplets. *Computers & Fluids*, 38(6), pp.1191-1202.

4.   Kompinsky, E. and Sher, E., 2009. Experimental comparisons between droplet-droplet collision and single-droplet impacts on a solid surface. *Atomization and Sprays*, 19(5).

5.   Abbott, C.E., 1977. A survey of waterdrop interaction experiments. *Reviews of Geophysics*, 15(3), pp.363-374.

6.   Orme, M., 1997. Experiments on droplet collisions, bounce, coalescence and disruption. *Progress in Energy and Combustion Science*, 23(1), pp.65-79.

7.   Eggers, J., Lister, J.R. and Stone, H.A., 1999. Coalescence of liquid drops. *Journal of Fluid Mechanics*, 401, pp.293-310.

8.   Estrade, J.P., Carentz, H., Lavergne, G. and Biscos, Y., 1999. Experimental investigation of dynamic binary collision of ethanol droplets–a model for droplet coalescence and bouncing. *International Journal of Heat and Fluid Flow*, 20(5), pp.486-491.

9.   Qian, J. and Law, C.K., 1997. Regimes of coalescence and separation in droplet collision. *Journal of Fluid Mechanics*, 331, pp.59-80.

10.   Jiang, Y.J., Umemura, A. and Law, C.K., 1992. An experimental investigation on the collision behaviour of hydrocarbon droplets. *Journal of Fluid Mechanics*, 234, pp.171-190.

11.   Yi, N., Huang, B., Dong, L., Quan, X., Hong, F., Tao, P., Song, C., Shang, W. and Deng, T., 2014. Temperature-induced coalescence of colliding binary droplets on superhydrophobic surface. *Scientific reports*, 4, p.4303.

12.   Peng, K., Wu, Y., Fang, H., Zhong, X., Xu, Y. and Zhu, J., 2005. Uniform, axial-orientation alignment of one-dimensional single-crystal silicon nanostructure arrays. *Angewandte Chemie International Edition*, 44(18), pp.2737-2742.

13.   Coffinier, Y., Janel, S., Addad, A., Blossey, R., Gengembre, L., Payen, E. and Boukherroub, R., 2007. Preparation of superhydrophobic silicon oxide nanowire surfaces. *Langmuir*, 23(4), pp.1608-1611.

14.   Vargaftik, N.B., Volkov, B.N. and Voljak, L.D., 1983. International tables of the surface tension of water. *Journal of Physical and Chemical Reference Data*, 12(3), pp.817-820.

15.   Aarts, D.G., Lekkerkerker, H.N., Guo, H., Wegdam, G.H. and Bonn, D., 2005. Hydrodynamics of droplet coalescence. *Physical review letters*, 95(16), p.164503.

16.   Rayleigh, L., 1879. On the capillary phenomena of jets. Proc. R. Soc. London, 29(196-199), pp.71-97.

17.   Kestin, J., Sokolov, M. and Wakeham, W.A., 1978. Viscosity of liquid water in the range− 8 C to 150 C. *Journal of Physical and Chemical Reference Data*, 7(3), pp.941-948.

18.   Koo, J. and Kleinstreuer, C., 2004. Viscous dissipation effects in microtubes and microchannels. *International Journal of Heat and Mass Transfer*, 47(14-16), pp.3159-3169.

19.   Hunter, S.C., 1957. Energy absorbed by elastic waves during impact. *Journal of the Mechanics and Physics of Solids*, 5(3), pp.162-171.

20.   Lenz, P., 1999. Wetting phenomena on structured surfaces. *Advanced Materials*, 11(18), pp.1531-1534.

Chapter 5. Conclusions

Conclusions

The thesis has shown the studies on the interaction between water droplets and superhydrophobic surfaces from static behaviours to dynamic. Nature of the surface, including water contact angle and surface morphology, and temperature of the droplet were studied and found to be two of the major factors which dominate the droplet behaviour.

The idea at the very beginning was simple and intuitive – nature of the surface was considered because it is what makes a superhydrophobic surface. The effect of droplet temperature is also significant and obvious, as the influences such as higher diffusion rate, heat transfer and surrounding vapor could be observed in daily life.

The work started from the synthesis of superhydrophobic surfaces with a gradient of water contact angles and surface structures. In Chapter 2, a new fabrication method of superhydrophobic thin films was first reported. The method includes an immersion step to modify the Co_3O_4 surface with stearic acid, during which the surface morphology was found to evolve on a time-dependent basis. Hence a theoretical investigation was conducted into the relationship between the contact angle, sliding angle, droplet size and micro- and nano- structures. As a result, it is feasible to effectively manipulate the surface adhesion by tailoring the surface morphology, which is simple in this case.

In Chapter 3, the dynamic process of evaporation of sessile water droplets was studied at different static water contact angles on hydrophobic and superhydrophobic substrates. The process was assumed to follow CCR mode and CCA mode successively. Energy factors were also taken into account by considering the effect of temperature and evaporative cooling. By combining the experimental result and

theoretical understanding, the lifetime of evaporation was believed to increase as surface contact angle rises whereas it decreases when the temperature rises. The contact angles where the evaporation mode transits on different surfaces were also obtained.

In Chapter 4, the process and the droplets themselves were both dynamic. With the help of high-speed camera, the coalescence/rebound process of binary droplets on superhydrophobic surface was researched. A droplet was set on a Si-based superhydrophobic surface while another was released from above to make a head-on collision. Series of merging/rebounding evolution images were captured by changing the temperature of the incoming droplet. Considering the influence of surrounding vapour at high temperature and the energy conversion in the process, it was revealed that an increase in the temperature of the impacting droplet smoothed the coalescence process between the binary droplets.

Schemes below show a small summary of the chapters in this thesis.

Chapter 1. Introduction

Water droplets on solid surfaces: wetting and partial-wetting

The Lotus Effect

Micro- and nano- structures + hydrophobic wax

Surface tension

Superhydrophobic surfaces

Contact angle

Sliding angle

Contact angle hysteresis

Fabrication

Application

Young's model
Wenzel model
Cassie-Baxter model

Roughen low surface energy materials

Modify a rough surface with low surface energy materials.

Self-cleaning
Oil-water separation
Anti-icing
Anti-bacteria
...

Fig. 5.1 Summary of Chapter 1.

Chapter 2. Synthesis of superhydrophobic surfaces with Wenzel and Cassie–Baxter state

Step 1. Immersion: $Co(NO_3)_2 \cdot 6H_2O + CO(NH_2)_2 = Co_3O_4$ nano-structures

13h   16h   18h   20h

SEM
TEM

Nanowires

Initial formation of nano-flowers

Increased number and size of nano-flowers

Completely covered by nano-flowers

Step 2. Modification by stearic acid

XRD
XPS

Superhydrophobic film

Static contact angle:

Droplets volume:
no significant influence

Roughness:
r↓ θ ↓

Sliding angle:

Droplets volume:
$sin\alpha \propto \frac{1}{V^{\frac{1}{3}}}$
Roughness:
r↓ α ↑
or α ↑ ↑ if partly in Wenzel state

Fig. 5.2 Summary of Chapter 2.

Chapter 3. Lifetime of droplets evaporation on hydrophobic surfaces

Experimental:

Preparation: substrates with different contact angles

Different substrates and temperatures

Evaporation: droplets lifetime data

θ_t , where CCR stage transits to CCA

Theoretical fitting:

CCA
t_{CCA-PB}
t_{CCA-E}

CCR
t_{CCR-M}

t_{total}

Evaporative cooling

Assumption: pure CCR followed by pure CCA

B_o, C_a: the droplet can be treated like a spherical cap.

Characteristic diffusion time: the process is governed by the droplet evaporation time.

Fig. 5.3 Summary of Chapter 3.

Chapter 4. Binary Impacting droplets on superhydrophobic surface

Experimental:

Preparation: superhydrophobic silicon plate
via silver assisted etching followed by salinization with fluorosilane

'Static' droplet with different temperatures

Binary droplet impact: photos by high-speed camera

Temperature-dependent deformation before coalescence

Surface contact time

Energy conversion and dissipation

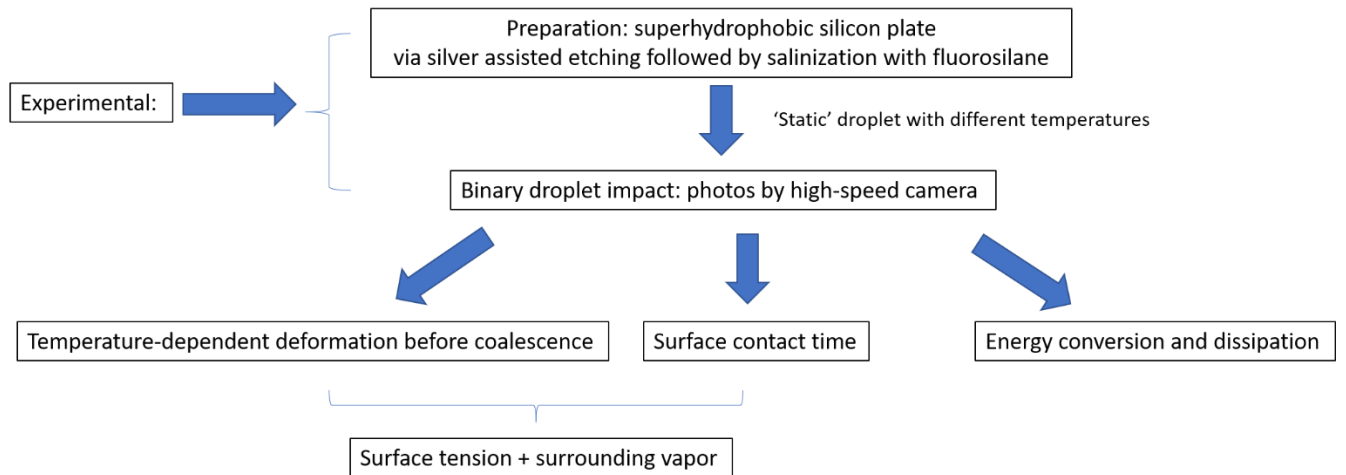Surface tension + surrounding vapor

Fig. 5.4 Summary of Chapter 4.

Future work

Some of the complementary and further researches to be done in the future includes:

1. Broadening the range of temperature in the studies.

Due to the limit of facilities it was difficult to conduct tests below room temperature in the experiments of evaporation and binary droplets collision. However, the results are still important to extrapolate the conclusions. A cooling device might be used to create the conditions for lower temperature experiments.

The upper limit can also be increased to the boiling point. In addition, the vaporization properties of water droplets near the Leidenfrost Point on superhydrophobic surfaces will be studied.

2. Increasing the experimental precision.

For example, in Chapter 4, the time point of coalescence of two droplets was determined by observation of both merging liquid boundary and dye diffusion. The result would be more accurate if some more obvious 'signs' could be adopted.